A revised oxygen barometry in sulfide-saturated magmas and application to the Permian magmatic Ni–Cu deposits in the southern Central Asian Orogenic Belt

Ya–jing Mao, Ke–zhang Qin, Stephen J. Barnes, Clément Ferraina, Giada Iacono-Marziano, Michael Verrall, Dongmei Tang, Shengchao Xue

A revised oxygen barometry in sulfide-saturated magmas and application to the Permian magmatic Ni–Cu deposits in the southern Central Asian Orogenic Belt

Ya–Jing Mao[a,b*], Ke–Zhang Qin[a,d], Stephen J. Barnes[b], Clément Ferraina[c], Giada Iacono–Marziano[c], Michael Verrall[b], Dongmei Tang[a], Shengchao Xue[e]

[a] Key Laboratory of Mineral Resources, Institute of Geology and Geophysics, Chinese Academy of Sciences, Beijing 100029, China

[b] CSIRO Mineral Resources, Perth, 6151, Australia

[c] ISTO, UMR 7327 CNRS-Université d'Orléans–BRGM, 1A rue de la Ferollerie, 45071 Orléans Cedex 2, France

[d] University of Chinese Academy of Sciences, Beijing 100049, China

[e] State Key Laboratory of Geological Processes and Mineral Resources, China University of Geosciences, Beijing 100083, China

Mineralium Deposita

[*]corresponding author: Ya–Jing Mao, maoyajing@mail.iggcas.ac.cn

Abstract

Oxygen fugacity is a key parameter in controlling the petrogenesis of the mafic-ultramafic rocks and their associated sulfide mineralization, especially in convergent settings. This study uses new and previously published experimental data on olivine-sulfide pairs to reparametrize an expression for oxygen barometry using the distribution coefficient K_D^{FeNi} for Fe-Ni exchange between olivine and sulfide. We derive a new expression, $\Delta QFM = (9.775 + 0.416 \cdot C_{Ni} - K_D^{FeNi}) / 4.308$, where ΔQFM denotes divergence from the fayalite–magnetite–quartz buffer. The revised oxygen barometry has been applied to the Permian magmatic Ni–Cu deposits in the Central Asian Orogenic Belt, NW China. The Ni–Cu deposits in the East Tianshan-North Tianshan, Central Tianshan, and Beishan-are considered as a single mineral system, whereas the spatially separated deposits in the East Junggar are considered as a separate system. The deposits of the East Tianshan group exhibits a large range of oxygen fugacity (QFM–2 to ~QFM +1) and Ni tenor (metal concentration in pure sulfide, ~5 wt.% to 16 wt.%). The Poyi and Huangshannan deposits in east Tianshan contain high Ni tenor sulfides, varying from 12 to 16 wt.%. The relatively high Fo values (>85 mol.%) and Ni contents (>2000 ppm) in olivine of these deposits indicate that the high Ni tenor sulfides were segregated from less differentiated high-Ni magmas that also had relatively high oxygen fugacity (~QFM +1). The remaining Ni–Cu deposits in east Tianshan - the Huangshandong, Huangshanxi, Hulu, Tulaergen, Tudun, and Xiangshanzhong deposits - have intermediate Ni tenors (5–8 wt.%). These sulfides

correspond to the intermediate Fo values (80–84 mol.%) and Ni contents (700–1400 ppm) in the coexisting olivine, illustrating that they were segregated from magmas with lower Ni contents thought to be the result of a large amount (15-20%) of olivine fractionation at depth. These magmas are more reduced ($-2 < \Delta QFM < +0.3$) than the less evolved magmas (~QFM +1). It is shown that ΔQFM value calculated for the deposits in east Tianshan decreases with the decreasing Fo value, indicating that the host magmas became gradually reduced during evolution, which can be explained by primarily oxidizing magma progressively assimilating crustal material containing reducing agents, such as graphite. The Kalatongke deposit in the East Junggar belt, containing the lowest Ni tenors in sulfides (3–5 wt.%) and low Fo values in olivine (<78 mol.%), was derived from relatively oxidizing magmas (~QFM + 1) that probably have experienced significant olivine plus clinopyroxene and plagioclase fractionation at depth. We propose that the variation in oxygen fugacity and Ni tenor in the Permian Ni–Cu deposits in the CAOB is the result of gradual contamination and a variable degree of fractional crystallization.

Key words: Magmatic sulfide deposit, Oxygen barometer, Sulfide-olivine Fe-Ni exchange, Nickel tenor, Central Asian Orogenic Belt

Introduction

Sulfur speciation in magma is controlled by its oxidation conditions. Strongly

64 oxidized magma will dissolve S as sulfate rather than sulfide (Jugo et al., 2009), giving
65 rise to much higher S contents at sulfate rather than sulfide saturation. This variable
66 may be critical in forming Ni–Cu deposits in convergent settings due to the relatively
67 oxidized character of partial melts derived from supra-subduction zone mantle (Frost
68 and McCammon 2008). Numerous experimental studies of iron and nickel partitioning
69 between olivine and sulfide liquid under magmatic conditions (Brenan 2003; Brenan
70 and Caciagli 2000; Fleet and MacRae 1988; Gaetani and Grove 1997) demonstrate that
71 the oxygen fugacity (fO_2), or more precisely the ratio of ferric to ferrous iron in the
72 magma for which fO_2 is a proxy, plays a role in determining compositions of olivine
73 and coexisting sulfide liquid. The Fe–Ni equilibrium between sulfide and coexisting
74 olivine is often expressed as an exchange coefficient (K_D):

75 $$K_D = (X_{NiS}/X_{FeS})_{\text{sulfide liquid}}/(X_{NiO}/X_{FeO})_{\text{olivine}} \quad (1)$$

76 where *Xi* is equal to the mole fraction of component *i* in the phase of interest.
77 Brenan and Caciagli (2000) found that K_D is a function of both fO_2 and sulfide melt Ni
78 content and that the variation in K_D recorded by natural samples can be reconciled in
79 terms of changes in both these parameters at the magmatic stage. K_D can be estimated
80 using the compositions of olivine and the coexisting magmatic sulfide assemblage in
81 natural systems and be used as an indicator of their oxidation state (Barnes et al. 2013;
82 Brenan and Caciagli 2000). However, experimental data that have yielded at relatively
83 oxidizing and low Ni tenor in sulfide are rare.

84 The magmatic Ni–Cu deposits in the Central Asian Orogenic Belt (CAOB), NW

China, were emplaced within an orogenic belt at the post–subduction stage (Li et al. 2012; Qin et al. 2011; Song et al. 2013; Su et al. 2011), in contrast to the more typical intra-plate craton margin setting of Ni–Cu dominant magmatic sulfide deposits (Maier and Groves 2011). Deposits in convergent-margin orogenic belts have received increasing attention after the discovery of some substantial Ni–Cu deposits in such settings, such as the Nova Ni–Cu deposit in Albany–Fraser belt in western Australia (Maier et al. 2016) and the Xiarihamu Ni–Cu deposit in Tibet plateau in west China (Li et al. 2015). The cluster of Ni–Cu deposits in NW China offer a great opportunity to study the oxygen fugacity and its controlling factor of the Ni–Cu deposits in such tectonic setting. Zircon U–Pb studies reveal that the majority of these intrusions in NW China were emplaced during the Permian (Qin et al. 2011; Su et al. 2011). These Permian Ni–Cu deposits contain ~300 Mt reserves at average grades of 0.5 wt.% Ni and 0.3 wt. % Cu, representing one of the most important Ni provinces in China (Mao et al. 2008). Although these deposits occur in different tectonic terranes, representing different accretionary arcs or micro–continents (Jahn 2004; Xiao et al. 2009), they have several similarities in terms of emplacement age, geochemical features, and thus source characteristics (Deng et al. 2014; Gao and Zhou 2013; Han et al. 2004; Li et al. 2012; Mao et al. 2014a; Mao et al. 2016; Qin et al. 2011; Song and Li 2009; Su et al. 2011; Sun et al. 2013b; Tang et al. 2011; Tang et al. 2013; Xue et al. 2016; Zhang et al. 2009; Zhou et al. 2004). Nevertheless, there are also several differences among these deposits, such as host rocks, sulfide textures, Ni and platinum group elements (PGEs) tenors in

106 sulfides, and olivine compositions (Mao et al. 2017; Qin et al. 2012; Su et al. 2013).
107 The close spatial and tectonic association of these deposits makes them a good case
108 study for a series of deposits forming part of a single mineral system, having a probable
109 derivation from a common mantle source, but undergoing different paths towards
110 emplacement.

111 In this study, a revised equation is presented for the fO_2 dependence of the
112 olivine/sulfide Fe/Ni K_D based on a revised calibration using some new experimental
113 data. The Permian Ni–Cu deposits in east Tianshan are considered as components of a
114 single mineral system. The revised equation is applied to the Permian deposits, using
115 the technique of microbeam XRF mapping to estimate the Ni tenor of the sulfide
116 component of these deposits. Integrating these data with the coexisting olivine
117 composition, we estimate the oxygen fugacity and Ni tenor variations of these deposits
118 and their controlling factors. The major aim of the contribution is to understand the
119 processes that control the variability of oxygen fugacity and Ni tenor of the magmatic
120 Ni–Cu systems in orogenic belts, using a series of comagmatic deposits forming part
121 of a single mineral system.

122 **Overview of the Permian magmatic Ni–Cu deposits in NW China**

123 Economic Ni–Cu deposits discovered to date in the CAOB are restricted to the
124 southern margin, including the Hongqiling No.7 deposit in NE China and the cluster of
125 Ni–Cu deposits in NW China (Fig. 1). The most important discovery of Ni–Cu deposits
126 in NW China, the Huangshandong and Huangshanxi deposits in the North Tianshan and

127 the Kalatongke deposit in the East Junggar (Table 1), was made in the 1980s (Wang and
128 Zhao 1991; Wang et al. 1987). Subsequently, a number of other mafic-ultramafic
129 intrusions were found to host magmatic sulfides, such as the Xiangshan, Huangshanxi,
130 Tudun, and Hulu deposits (Table 1). In the 2000s, some additional discoveries were
131 made such as the Tulaergen deposit in the east part of North Tianshan (San et al. 2003)
132 and the Baixintan occurrence in the west part of North Tianshan (Li et al. 2014) (Fig.
133 2). In addition, economic Ni–Cu ore bodies had been outlined in the Poyi and Poshi
134 mafic–ultramafic intrusions in the Beishan Terrane (Xia et al. 2013). The Permian
135 emplacement age of the Huangshandong, Huangshanxi, and Kalatongke deposits was
136 first established by Han et al. (2004) and Zhou et al. (2004) using zircon U–Pb dating.
137 The main features of some of these deposits have been reviewed by Mao et al. (2008)
138 and Lightfoot and Evans–Lamswood (2015). Between 2008 and 2016, numerous case
139 studies, including precise dating, whole rock geochemical analysis and studies of
140 mineral composition and PGE concentrations have been carried out on these Ni–Cu
141 deposits (Zhang et al. 2009, 2011; Tang et al. 2011; Sun et al. 2013a; Deng et al. 2014;
142 Mao et al. 2014a, 2015; Yang et al. 2014; Zhao et al. 2015; Xue et al. 2016).

143 The Ni–Cu deposits in NW China mainly occur in four terranes, the Beishan,
144 Central Tianshan, North Tianshan and East Junggar from south to north (Fig. 2). The
145 Beishan, Central Tianshan, and North Tianshan terranes are named as east Tianshan in
146 this study. The Beishan Terrane is located in the northeastern part of the Tarim craton,
147 adjacent to the Central Tianshan Terrane in the north (Fig. 2). It is mainly composed of

148 the Precambrian crystalline basement and overlying sedimentary rocks, namely
149 Archean granitic gneiss, Paleoproterozoic amphibolite, gneiss, schist, quartzite, and
150 marble, overlain by Carboniferous volcanic and sedimentary rocks (BGMRXUAR
151 1993). Magmatic sulfide–bearing mafic–ultramafic intrusions, such as the Poyi and
152 Poshi Ni–Cu deposits, the Bijiashan, Xuanwoling, and Hongshishan occurrences, are
153 widespread in the Beishan Terrane. Most of those intrusions are characterized by minor
154 Ni–Cu mineralization with low Ni grade and high proportions of olivine (Su et al. 2013;
155 Xia et al. 2013; Xue et al. 2016). Olivines in these intrusions tend to have high forsterite
156 (Fo) values and high Ni contents, significantly higher than those in neighboring terranes.
157 The Central Tianshan Terrane is composed of the Precambrian crystalline basement
158 including the Mesoproterozoic Xingxingxia Group and Kawabulak Group. These
159 Groups are dominated by gneisses, schists, marbles, and phyllites (BGMRXUAR,
160 1993). The Tianyu and Baishiquan are two mineralized intrusions in the Central
161 Tianshan (Chai et al. 2008; Tang et al. 2011). The North Tianshan Terrane is dominated
162 by well–developed Devonian–Carboniferous strata, granites, and mafic–ultramafic
163 complexes (BGMRXUAR, 1993). The lower Devonian to lower Carboniferous rocks
164 mainly comprise sandstone, pelitic slate, siltstone, mudstone, pyrite–bearing mudstone,
165 and limestone. The middle to upper Carboniferous strata is composed of mafic to
166 intermediate volcanic rocks with abundant chert and limestone. The Baixintan Ni–Cu
167 occurrence is located in the west part of the North Tianshan. A number of economic Ni–
168 Cu deposits, e.g. the Huangshandong, Huangshanxi, Huangshannan, Xiangshanzhong,

and Tudun deposits occur in the central part (Huangshan camp), whereas the Tulaergen and Hulu deposits occur in the east part (Fig. 2). The Xiangshanzhong deposit represents the central part of the Xiangshan complex, which has been divided into three parts from west to east: the Xiangshanxi Ti–Fe mineralized segment, Xiangshanzhong Ni–Cu related segment, and Xiangshandong currently sulfide barren segment. The East Junggar orogenic belt comprises several metasedimentary and ophiolite assemblages, dominated by the Devonian rocks consisting of calc–alkaline volcanics and marine clastic sediments overlain by thick Carboniferous marine clastic sedimentary successions (BGMRXUAR 1993). The Kalatongke mafic intrusion is the only economic Ni–Cu deposit in the East Junggar (Fig. 2), but a few small Permian mafic–ultramafic intrusions with Ni–Cu mineralization close to the Kalatongke intrusion have been discovered in the 2010s, e.g. the Kemozibayi intrusion.

The common features of the Permian Ni–Cu deposits are as follow: (1) Small intrusions in size with surface area less than 3 km^2, showing a spectrum of morphologies including rhomboid–shaped funnels, dyke–sill transitions and oblate channels (Barnes et al. 2016; Lightfoot and Evans-Lamswood 2015; Qin et al. 2012); (2) The intrusions are within strike–slip transtensional zones and are located at jogs or cross–linking structures, forming in open systems by multiple magma pulses (Lightfoot and Evans-Lamswood 2015; Mao et al. 2014b); (3) intrusions from the different tectonic terranes were emplaced within a narrow range of ages, from 270 to 290 Ma (Qin et al. 2011), coeval with the flood basalt in the Tarim craton (Tian et al. 2010); (4) The occurrence

of hydrous minerals, such as hornblende, phlogopite, and biotite in some intrusions, together with the arc–like geochemical character, suggesting the parental magmas were derived from a mantle source previously metasomatized by slab–derived fluids (Mao et al. 2015; Su et al. 2011); (5) crustal contamination, probably crustal sulfide contamination, is the key factor in triggering sulfide saturation (Mao et al. 2016; Xue et al. 2016); (6) the sulfide assemblage is dominated by pentlandite, pyrrhotite, and chalcopyrite, and PGE contents in these sulfides are low (Mao et al. 2017; Tang et al. 2011; Xue et al. 2016; Yang et al. 2014).

Apart from the Kalatongke deposit, which has relatively high Ni and Cu grades (0.6–0.9 wt.% for Ni and 1.1–1.4 wt.% for Cu), the other Ni–Cu deposits in NW China are of low Ni and Cu grades (Table 1). The Ni–Cu mineralization of these deposits occurs in both ultramafic rocks (dunite, lherzolite, olivine websterite) and mafic rocks (olivine gabbronorite, gabbronorite, gabbro). The deposits related to mafic rocks tend to have higher sulfur abundances than those related to ultramafic rocks. For mineralization associated with ultramafic rocks, such as the Huangshandong (ultramafic unit), Huangshanxi, Huangshannan, and Poyi intrusions, the sulfide textures are dominated by disseminated texture (sulfide content less than 20 wt.%), with minor net–textured and massive textures (less than 20%, Fig. 3). In contrast, mineralization associated with the mafic rocks, e.g. the Huangshandong mafic unit and Kalatongke deposits, has a wide range of sulfide textures. Net–textured and massive textures are the dominant ores in these deposits, whereas the disseminated ore accounts for less than

211 30 % (Fig. 3).

212

213 **Experimental and analytical procedures**

214 *Experimental and analytical methods of Fe-Ni exchange between olivine and sulfide*

215 A picritic gabbro-dolerite (from Noril'sk 1 intrusion) was used as starting material
216 for our experiment. The rock was powdered and melted at 1600 °C and atmospheric
217 pressure for 2 hours into a homogenous volatile-free glass. Experiments were
218 conducted in internally heated pressure vessels equipped with a rapid quench device at
219 1200 ± 2 °C, 66 ± 2 MPa during 1 to 3 hours at the CNRS-ISTO, France (Table 2). The
220 powdered starting glass was loaded into Pt capsules (internal diameter 5.7 mm) with
221 the addition of 2 wt.% H_2O and 5 wt.% S. The fO_2 varied between –0.78 and 2.11 log
222 units relative to the QFM buffer, by adapting the partial pressure of hydrogen in the
223 vessel. The redox solid sensor method (Co-Pd–CoO; Taylor et al., 1992) was also
224 employed to check the fO_2: two pellets of CoPd metal mixtures and CoO were placed
225 in a Pt capsule in the presence of excess H_2O, and run at the same time of the samples,
226 but for a longer duration (3-4 days, in order to reach the equilibrium). The fO_2 of the
227 sensor is determined by the composition of its metallic phases, following Taylor et al.
228 (1992), and the fO_2 of each charge then calculated following Botcharnikov et al. (2008)
229 considering the activity of H_2O estimated for every charge. Calculated fO_2 are presented
230 in Table 2. Every capsule was verified to have remained sealed during the experiments

by checking its weight after the experiment. The capsules were then cut half along their long axis, mounted in epoxy resin and polished for further analysis.

Olivine crystals and sulfide globules in each experimental sample were recognized by scanning electron microscopy (ZEISS Merlin compact FEG-SEM at CNRS-ISTO, France), and analyzed for their major element composition and Ni contents by electron microprobe (Cameca SX Five at CNRS-ISTO, France). Operating conditions for both sulfide and olivine were 20 kV accelerating voltage, 30 nA beam current, 10 s peak counting time for each element, except Ni for olivine (120 s), and O for sulfides (120 s). A focused beam was used for olivine, whereas the size of the spot was adapted to that of the sulfide droplet. Standards deviations for major elements in olivines and Fe, S concentrations in sulfide are less than 5 %. For Ni in sulfides, standard deviations are less than 20 % in samples containing more than 1 wt.% Ni in sulfide. Nickel content in olivine shows a more important variation (between 30 and 70 %) due to the low values close to the detection limit (i.e. ~ 100 ppm). Sulfur fugacity (fS_2) was calculated from the experimental temperature, pressure, fO_2 and total FeO content of the silicate melt, using the equation in Mungall and Brenan (2014).

Analysis of olivine and pentlandite compositions of natural samples

Olivine analyses in this study were obtained from polished thin sections of the mineralized samples. The composition of olivine from the Xiangshanzhong deposit was obtained by wavelength–dispersive microprobe analysis using a JEOL JXA8100

electron probe at the Institute of Geology and Geophysics, Chinese Academy of Sciences. The operating conditions were 15 kV accelerating voltage, 12 nA beam current, 5 μm beam size and 30 s peak counting time. Nickel and Ca in olivine were analyzed using a beam current of 20 nA and a peak counting time of 100 s. The detection limit for Ni and Ca under such conditions is ~200 ppm. The composition of olivine from the Kalatongke and Tudun deposits were analyzed at the Centre for Microscopy, Characterization and Analysis, The University of Western Australia, using a JEOL JXA8530F electron microprobe equipped with five tunable wavelength dispersive spectrometers. Operating conditions were 40 degrees take–off angle, a beam energy of 20 keV, a beam current of 150 nA and a peak counting time of 100 s. The detection limit for Ni and Ca under such conditions is ~50 ppm.

Nickel, Fe, Co, and S contents in pentlandite were determined by scanning electron microscope-based energy dispersive spectrometry (SEM-EDS), at CSIRO, Perth. SEM-EDS analyses were performed on carbon–coated, polished thin sections using a Zeiss Ultra–Plus field emission gun (FEG) SEM coupled with a Bruker X–Flash energy dispersive X–ray (EDX) detector for elemental analyses. An accelerating voltage of 20 kV and a beam current of 3 nA were used. The analysis time per analyses was set as 120 seconds. The coefficient of variations of Fe, S, and Ni contents in pentlandite yielded from repeated analysis on the same pentlandite grain are less than 1.1%, whereas the coefficient of variation of Co content in pentlandite is less than 4.5 %.

Calculation of sulfide composition using XRF images

The images of sulfide bearing samples used for 100% sulfide composition calculations were obtained using the desktop X–ray fluorescence M4 Tornado™ instrument at CSIRO, Perth, equipped with a rhodium target X–ray tube operating at 50 kV and 500 nA without filters and an XFlash® silicon drift X–ray detector. Maps were created using a 40 μm spot size on a 40 μm raster with dwell times of 10 ms per pixel. Maps are represented as un–quantified background–corrected peak height data for Kα peaks for each element, scaled linearly between minimum and maximum measured counts over the sample. Image processing software, ImageJ (version 1.50i), was used to analyze the modal proportions of sulfide minerals, based on the S, Cu, Ni single elemental distribution (S, Cu, and Ni representing the proportion of pyrrhotite, chalcopyrite, and pentlandite, respectively). The weight percentages of pentlandite, chalcopyrite, and pyrrhotite in sulfides were calculated based on the volume proportions of the sulfide minerals, assuming the density of pentlandite, chalcopyrite, and pyrrhotite as 4.8 g/cm^3, 4.2 g/cm^3, and 4.7 g/cm^3, respectively. These results, together with pentlandite and pyrrhotite compositions yielded from SEM-EDS, were used to estimate the weight percentages of Ni, Cu, and Fe in the 100% sulfide composition. In the calculation, we used a uniform pyrrhotite composition of $Fe_{0.9}S$ for all of the deposits according to SEM-EDS analysis, and assumed the Cu is distributed in standard formula chalcopyrite. The sulfide assemblage has been observed to be chalcopyrite, pyrrhotite, and pentlandite in all the deposits.

Before analyzing the proportion of pentlandite and chalcopyrite, two steps are necessary to precisely estimate the sulfide composition using XRF images. Firstly, applying a threshold to Cu and Ni images to decrease the X–ray signal derived from beneath the sample surface and/or the background, which may cause overestimate of the Ni and Cu tenors. Although most of the Ni and Cu are consistently distributed within S, some Ni and Cu occur outside of the sulfur region (Fig. 4), probably resulting from Ni and Cu signal from sulfide beneath the sample surface. Thus, we created an inverse of the S image, a "non–S", which was then subtracted to the Cu and Ni images, yielding modified Cu and Ni images. This step restricts the Cu and Ni signals to these originated from the sample surface, consistent with the S signal that derives from the surface. Subsequently, S image was combined with modified Cu and Ni images and the areas of these three elements represent the 2D volume proportions of chalcopyrite, pentlandite, and pyrrhotite.

The calculated Ni tenors of the Tudun and Huangshanxi deposits using this method, at both hand–sample and thin–section scales (Fig. 5), are consistent with the Ni contents calculated for 100% sulfide from measured S, Cu, and Ni concentrations in whole rock (Mao et al. 2014a). The error of Ni tenor calculated using these two methods are within 1 wt.% for most of the samples (Fig. 5a). For sulfides from NW China, the results of Ni tenor calculated by XRF images at thin section scales are comparable to these estimated by whole rock data of hand sample size. On the other hand, Cu contents in sulfides calculated by XRF images at thin–section scale tend to be more scattered than

313 these estimated at hand–sample scale as well as these by whole rock compositions (Fig.
314 5b). This may be due to the mobility of Cu at both late magmatic and hydrothermal
315 stages. However, the calculated Cu contents in sulfides at thin section scale are within
316 2 wt.%. In addition, the samples chosen for the comparison have sulfur contents varying
317 from 0.87 wt.% to 4.6 wt.%, representing low-grade ores. The Ni tenors in sulfides
318 yielded from XRF images (Fig. 4) agree with those calculated by whole rock S, Ni, Cu
319 data (Fig. 5). The advantage of sulfide composition estimation using the XRF image
320 compared to the traditional calculation based on the whole rock composition is
321 primarily that it removes the large uncertainty in the silicate Ni background for sulfide
322 samples (S<2 wt.%), which is the primary source of uncertainty in the calculated metal
323 tenors (Barnes et al. 2011).
324

325 **Results**

326 *Experimental results of Fe-Ni exchange between olivine and sulfide*

327 The experimental products consisted of glass, olivine crystals, sulfide globules
328 (Fig. 6), and minor gas bubble (Fig. 6b). The sulfide globules represent a quenched
329 sulfide melt that segregated from the picritic melt (Fig. 6). The homogenous
330 composition of all the phases (Table 2) attests the attainment of equilibrium. Our
331 experiments, conductedformat oxygen fugacities between QFM –0.8 and QFM +2.1,
332 explore the most oxidizing condition of the existing experimental database (Fig. 7; Fleet

and MacRae 1988; Gaetani and Grove 1997; Brenan and Caciagli 2000; Brenan 2003). The sulfides present Ni tenor from 0.8 to 7 wt.%, which are lowerthan previous data (Fig. 7). The K_D of Fe–Ni equilibrium between sulfide and coexisting olivine vary from 2.9 to 10.7, and are also among the lowest values of the dataset.

Sulfide melt compositions of the Permian Ni–Cu deposits

Compositional variation of pentlandite

It is necessary to determine the Ni content of pentlandite in order to determine the Ni tenor of the natural sulfide melts by the method applied here. The Ni and Fe contents in pentlandite range widely from deposit to deposit (Table 3). Pentlandite from the Kalatongke and Tudun deposits contain the highest Ni contents (35–37 wt.%) and lowest Fe contents (28–30 wt.%) of all the Ni–Cu deposits in NW China, with Ni/Fe ratios varying from 1.16 to 1.32. In contrast, pentlandite from the Poyi intrusion has relatively low Ni contents (27.5–32.5 wt.%) and high Fe contents (32.6–37.4 wt.%), with Ni/Fe ratios varying from 0.73 to 1. Other deposits, such as the Huangshanxi, Huangshandong, Huangshannan, and Xiangshanzhong, have medium Fe and Ni contents (29–32 wt.% and 32–34.5 wt.%, respectively) and Ni/Fe ratios (1.01–1.17) in pentlandite. In addition to Fe and Ni contents, Co contents in pentlandite vary significantly, from 0.6 to 0.9 wt.% at the Poyi and Huangshannan deposits and from 1.3 to 2.5 wt.% at other deposits.

353 Nickel and Cu tenors in sulfide melt

354 The Ni tenors of sulfides in the Poyi deposit (Table 4), estimated from XRF images
355 at both thin section and hand sample scales (Fig. 8), vary from 13.1 to 16 wt.%, which
356 is significantly higher than the estimate (average value of 8 wt.%) by Yang et al. (2014)
357 and slightly higher than the estimate (average value of 12 wt.%) by Xue et al. (2016).
358 The Ni tenors estimated by the previous studies are based on the whole rock Ni, Cu, S
359 concentrations. The inconsistency in Ni tenor yielded from these two methods is
360 probably due to the uncertainty of the correction of background Ni in olivine when
361 using the method based on whole rock S, Ni, and Cu contents. Since the mineralization
362 in the Poyi deposit is characterized by high proportion of olivine and low proportion of
363 sulfide (large proportion of mineralization contain less than 2 wt.% S contents), the
364 error of Ni tenors calculated by whole rock composition for these rocks may be
365 extremely high as pointed out by Barnes et al. (2011), owing to the fact that at small
366 sulfide proportions large uncertainties in the silicate Ni background are amplified into
367 very large uncertainties in the sulfide tenor. This component of uncertainty is avoided
368 by the direct sulfide mode measurement technique employed here. Our XRF results of
369 the sulfide compositions from the Poyi deposit show that these sulfides are comparable
370 with the high Ni tenor sulfides in the Huangshannan deposit (Mao et al. 2017). The
371 comparison suggests that the XRF images potentially provide a better way to calculate
372 Ni tenor for low–grade ores associated with high proportions of olivine.

373 The Ni tenors of samples from other deposits are well consistent with the published

374 data calculated from whole rock concentrations (Table 4). In contrast to the high Ni
375 tenor characteristic of the Huangshannan and Poyi deposits which contain high Ni/Cu
376 (2.5 to 7.3) but low Fe/Ni ratios (~3), sulfides from the Huangshanxi, Huangshandong,
377 Xianghsanzhong, Tudun, Tianyu, Hulu, and Tulaergen deposits have intermediate Ni
378 tenors (4–8.8 wt.%), Ni/Cu (0.9–2.5) and Fe/Ni (5.7–14) ratios. The sulfides from the
379 Kalatongke deposit are dominated by low Ni (~3.4 wt.%) but high Cu (~6.1 wt.%)
380 tenors, with Ni/Cu and Fe/Ni ratios varying from 0.1 to 0.9 and 15 to 38, respectively.
381 No systematic correlation is observed between Ni content in pentlandite and Ni tenor
382 in bulk sulfide, but the Ni/Co ratios of the Poyi and Huangshannan deposits (high Ni
383 tenor, shown below) are higher than 30, whereas those from other deposits (reduced Ni
384 tenor) are commonly less than 30.

385 *Olivine composition of the Permian Ni–Cu deposits*

386 Olivines in sulfide barren samples show a positive correlation between Fo value
387 and Ni tenor for the Ni–Cu deposits in NW China. Differently, olivines in mineralized
388 samples tend to show a negative correlation, such as the Poyi, Huangshannan,
389 Xiangshanzhong, Huangshanxi, and Kalatongke deposits (Fig. 9a), indicating
390 significant Fe–Ni exchange between sulfide and olivine. This negative correlation
391 arises during closed-system equilibration where most of the Ni in the system is in
392 sulfide; hence, as the Fe content of the olivine increases during reaction with trapped
393 liquid, the Ni content of the olivine also increases to satisfy the Fe-Ni exchange K_D

394 from equation 1 (Barnes and Naldrett 1985; Li et al. 2003).

395 Nevertheless, there is little difference in Fo variation between olivine from the
396 sulfide–bearing rocks and these from the sulfide–barren rocks. For clarity, we use the
397 average olivine composition for each deposit to the further comparison (Fig. 9b).
398 Generally, the Permian deposits have Fo values varying from 88 to 76.5 (Table 5). The
399 Huangshannan deposit in the North Tianshan and Poyi deposit from the Beishan
400 Terrane have relatively high Fo values (85.9–88 mol.%) and high Ni contents (2300–
401 2800 ppm), suggesting these deposits were formed by relatively unfractionated magmas.
402 On the other hand, the Kalatongke and Xiangshanzhong intrusions contain low Fo
403 values (76–79.5 mol.%) and relatively low Ni contents (1000–1300 ppm), illustrating
404 the parental magmas of these deposits are relatively evolved. The olivines from the
405 Huangshandong, Huangshanxi, Tudun, Tulaergen, Hulu, and Tianyu deposits contain
406 moderate Fo values (80–83.4) but variable Ni contents (670 to 1400 ppm). The olivines
407 from the Hulu and Tianyu deposits (intermediate Fo values, 80.4 and 83.4) are
408 significantly lower in Ni (average values of 780 and 600 ppm, respectively) than other
409 deposits.

410 There is a good positive correlation between Fo values in olivine and Ni tenor in
411 sulfide for these deposits, except the Huangshannan and Tulaergen deposits which
412 contain relatively higher Ni tenors than these having similar Fo values (Fig. 10). A
413 positive correlation is also evident between Ni in olivine and Ni in sulfide, the
414 Kalatongke low Ni tenor deposit being slightly outside of the main trend (Fig. 11a).

Commonly, high Ni tenor sulfides are associated with olivines with high Fo values (>86) and Ni contents (>2000 ppm). In addition, the Fe/Ni ratios in olivine (<50) from the high Ni tenor deposits are significantly lower than those from the relatively low Ni tenor deposits (>80) (Fig. 11b). The Cu/Ni ratios in sulfide tend to be higher than 1 for deposits consisting of olivine Fo values lower than 80, whereas Cu/Ni ratios are generally lower than 1 for deposits with olivine Fo values higher than 80 (Fig. 11c). The calculated exchange coefficient K_D of Fe–Ni equilibrium between sulfide and coexisting olivine of the Permian Ni–Cu deposits varies from 7.3 to 21.8 (Fig. 12). The K_D values of the Kalatongke, Huangshandong, Tudun, and Poyi deposits ($K_D < 13$) are slightly lower than these from the Huangshanxi, Tulaergen, Xiangshanzhong, Hulu, and Tianyu deposits ($K_D > 13$). The Kalatongke deposit in the East Junggar contains the lowest K_D and Ni tenor in sulfide, making it distinctly different from other coeval Ni–Cu deposits in east Tianshan (Tables 4, and 5, Figs. 11, and 12).

Discussion

Empirical equations to estimate the oxygen fugacity of sulfide– and olivine–saturated magmas

The equilibrium constant for the exchange of Fe and Ni between coexisting olivine and sulfide liquid (K_D) has been investigated in a number of experimental studies (Brenan 2003; Brenan and Caciagli 2000; Fleet and MacRae 1988; Gaetani and Grove

435 1997). In terms of the systematic dependence of K_D on fO_2, Ni tenor in sulfide (C_{Ni}),
436 and in some case fS_2, several empirical equations of K_D, fO_2, C_{Ni} have been proposed
437 (Barnes et al. 2013; Brenan and Caciagli 2000; Sciortino et al. 2015). Brenan and
438 Caciagli (2000) used a larger experimental database relative to previous studies (Fleet
439 and MacRae 1988; Gaetani and Grove 1997) and found the relationship between K_D
440 and log (fO_2) to be best described by a power–law relation. Barnes et al. (2013), using
441 the same experimental dataset, made the equation more applicable to model
442 calculations by replacing the log (fO_2) by ΔQFM (fO_2 relative to the quartz–fayalite–
443 magnetite oxygen buffer) and developed a polynomial equation relating K_D to C_{Ni}
444 (including a cubic term) and ΔQFM. This equation enables estimation of the oxygen
445 fugacity of the magma relative to QFM buffer, which is independent of the temperature.
446 Recently, Sciortino et al. (2015) recalibrated the same data set using only a linear term
447 for C_{Ni}, but also introducing a term for fS_2:

448 $$K_D = C_{Ni} \cdot [34.7 \cdot \log (fO_2 / fS_2) + 312] - 11 \cdot \log (fO_2 / fS_2) - 70.8 \qquad (2)$$

449 the revised equation (2) can well predict the fO_2 of the parental magma but requires
450 an estimate of fS_2 which is dependent on the silicate melt composition, equilibrium
451 temperature, and pressure. This formulation requires a complex parameterization of
452 these dependencies in order to obtain a solution, and is therefore difficult to access in
453 natural systems. Furthermore, this equation fails to apply to the new data in this study
454 (Fig. 13), when fS_2 is calculated using the equation in Mungall and Brenan (2014).

455 We added some new experimental data (Table 2) to the currently published dataset

(Brenan 2003; Brenan and Caciagli 2000; Fleet and MacRae 1988; Gaetani and Grove 1997) to calibrate a linear C_{Ni} and ΔQFM dependent equation for K_D. Our new experimental data using a picritic gabbro–dolerite as starting material represent the lowest Ni tenor in sulfide (1.5–1.8 wt.%), and the most oxidizing conditions (from QFM –0.78 to QFM +2.11) in the database (Table 2). The ultra–high K_D values (>40), which are commonly relating to ultra–high Ni content in sulfide (>50 wt.%), were not included in our calibration because of the poor linear relationship (Fig. 7). This will not influence the application of this equation to magmatic Ni–Cu systems due to the rarity of such compositions in nature. The relationship among K_D, sulfide melt compositions, and calculated ΔQFM was evaluated by multivariate linear regression analysis and is given by:

$$K_D = a + b \cdot C_{Ni} + c \cdot \Delta QFM \qquad (3)$$

In this equation, a, b, and c are constants which equal to 9.775, 0.416, and –4.308, respectively. The standard deviation of these constants is listed in Table 6 and the comparison of predicted K_D values between this equation and previous equations is present in Fig. 13. The average relative error of prediction for K_D using equation (3) is ±17.7% for all the data, similar to that of the equation (2) for the old data (±18.2%). The average error of prediction for ΔQFM using equation (3) is ±0.8 log unit ΔQFM for all the data.

Application of the empirical oxygen fugacity equation to the Permian Ni–Cu deposits in southern Central Asian Orogenic Belt

In the following discussion, the term "host magma" is used to represent the magma that was initially emplaced to form each individual intrusion, before in–situ fractionation within the intrusion, this term being equivalent to the term "parental magma" used in previous studies (Mao et al. 2015; Mao et al. 2014a; Sun et al. 2013b). Here we use "parental magma" to denote the most primitive host magma of the entire suite of Ni–Cu deposits in NW China, i.e. the magma that undergone the least fractionation and contamination after leaving the mantle source (primary magma).

The reverse correlations between Fo value and Ni content in olivine from mineralized samples (Fig. 9a) show that equilibrium of Fe and Ni exchange between olivine and sulfide were reached for the Permian Ni–Cu deposits. Based on the sulfide composition and K_D values of the sulfide bearing samples (Table 4), the ΔQFM values of the host magmas that were in equilibrium with sulfides (Fig. 14) were estimated using equation (3). Only samples with integrated olivine and sulfide compositions were used in the estimation. The samples which have undergone significant sulfide fractionation, i.e. anomaly Cu/Ni ratio (Table 4), were excluded from the oxygen fugacity calculation. For the Tianyu and Hulu deposit, which have no integrated olivine and sulfide compositions, the average composition of sulfides and olivine in disseminated to net-textured ores of these deposits were used to estimate the oxygen fugacity. The variations in oxygen fugacity of these two deposits are illustrated as error

496 bar, which is resulted from the variation in compositions of olivine and sulfides of these
497 deposits. The Poyi, Huangshannan, and Kalatongke intrusions were found to be
498 associated with the most oxidizing magmas in NW China, with oxygen fugacity at
499 around QFM +1. On the other hand, the other deposits (the Tianyu, Xiangshanzhong,
500 Tulaergen, and Huangshanxi deposits) are associated with relatively reduced magma
501 with fO_2 varying from QFM –2 to QFM +0.3. In the plot of ΔQFM values versus Fo
502 values in olivine (Fig. 14), the oxidation state of the host magma of the deposits in east
503 Tianshan decreases as the Fo values decrease, indicating that these host magmas
504 became gradually more reduced during the evolution.

505 *Origin of the oxygen fugacity variation in the host magmas*

506 Note that the ranges of fO_2 for individual deposit are commonly within one log
507 unit QFM, but the range of the fO_2 in the Huangshanxi deposit is significantly larger,
508 varying from ~QFM +1 to ~QFM –2. The extremely reducing oxidation state recorded
509 in the sample 06-18-944.3 (QFM –2) is not caused by sulfide fractionation (Table 4).
510 The high V/Sc and V/Ga ratios and heavy oxygen isotope enrichment in olivine of the
511 sample 06-18-944.3 relative to those of other samples in the Huangshanxi deposit (Mao
512 et al., in preparation) strongly suggest that the extremely reducing oxidation state in
513 sample 06-18-944.3 is the result of significant assimilation of graphite-bearing wall
514 rock. Furthermore, the relatively high oxidation state recorded in the Poyi and
515 Huangshannan Ni–Cu deposits, containing the most primitive olivines (Fo values

516 higher than 86 mol.%), suggests that the primitive magmas of these deposits are
517 characterized by relatively oxidizing condition. Such oxidation state of magmas is
518 consistent with that of spinel peridotites of the mantle wedge above the subduction zone,
519 which have oxygen fugacity of QFM +0.3 to QFM +2.0 (Frost and McCammon 2008;
520 Parkinson and Arculus 1999). The fact that all of these Permian deposits are
521 characterized by compositions of subduction zone affinity, i.e. significantly Nb and Ta
522 depletion relatively to Th and La, positive Pb and Sr anomalies (Deng et al. 2015; Li et
523 al. 2012; Mao et al. 2014a; Mao et al. 2016; Su et al. 2011), suggests that the magmas
524 were derived from extensively metasomatized supra-subduction zone mantle sources,
525 which may melt to form relative oxidizing magmas. Fractional crystallization modeling
526 of the host magma of the Poyi and Huangshannan deposits (Xue et al., 2016; Mao et
527 al., 2016) using MELTS (Asimow and Ghiorso 1998) predicts that the redox state of
528 these host magmas during olivine plus Cr-spinel fractionation should increase slightly
529 from QFM +1.2 to QFM +1.4, and from QFM +0.7 to QFM +1, respectively, at 1 kbar
530 pressure condition. The modeling results indicate that the fractionation is not the cause
531 of the progressive reduction for the fractionated host magmas. On the other hand, our
532 observed trend towards more reduced magmas with increasing fractionation (Fig 14) in
533 the east Tianshan intrusions could be the result of interaction with the relatively reduced
534 crustal materials. The assimilation of small amounts of organic matter (<1 wt.%) by
535 mafic-ultramafic magmas may dramatically decrease magma redox conditions (Iacono-
536 Marziano et al., 2012; 2017). For instance, the sulfide saturation of the parent magmas

537 to the Noril'sk–Talnakh Ni–Cu–PGE deposits is believed to have been triggered by
538 contamination of evaporite–bearing country rocks and organic matter from the country
539 rocks (Grinenko 1985; Li et al. 2003; Naldrett 2004; Iacono-Marziano et al. 2017). The
540 addition of evaporite increased the sulfate content of the parental magma, whereas the
541 input of reducing agents decreased the oxygen fugacity of the magma and reduced this
542 sulfate to much less soluble sulfide. In addition, in light of both isotopic and
543 petrographic evidence of the Voisey's Bay magmatic system (QFM–1 to QFM –3), a
544 model of magma reduction involving assimilation of graphite–bearing country rock by
545 a relatively oxidized parental magma has been explored (Brenan and Li 2000). The
546 ubiquitous occurrence of graphite–bearing tuff and graphite–bearing slate in the
547 Carboniferous wall rock of most of the mafic–ultramafic intrusions in the North
548 Tianshan and East Junggar terranes (Table 1, Fig. 2) may provide the reducing agents
549 to the magmas. The presence of xenolith of graphite-bearing wall rock in the
550 Huangshandong, Huangshannan and Huangshanxi intrusion (Wang et al., 1987)
551 suggests that the addition of carbonaceous material took place in these magmatic
552 systems. Thus, Ni–Cu deposits in the North Tianshan and the Beishan Terrane could be
553 the result of derivation from relatively oxidizing mantle source and became gradually
554 more reduced during the interaction with the wall rock. However, the absence of
555 graphite-bearing wall rocks in the Central Tianshan (Table 1) illustrates that the
556 relatively reduced feature of the Tianyu deposit is either the result of a relatively
557 reduced mantle source or addition of reducing agent to an oxidized magma at depth.

558 The latter scenario is possible due to the presence of Pre-Cambrian black shales in the
559 Central Tianshan Terrane (Table 1, Yang 2015).

560 Our observations raise the question of whether the addition of reducing agents is
561 necessary to trigger immiscible sulfide saturation in subduction-associated settings. The
562 fO_2 range controls sulfur speciation and hence maximum sulfur contents in the magma
563 during both source melting and sulfide segregation at the shallow crust, especially for
564 magmas generated in the arc, backarc, and island arc settings (Jugo 2009). During low
565 degree source partial melting, significantly oxidizing circumstances could generate
566 sulfide undersaturated primitive magma which may contain extremely high S content
567 as well as metal contents (such as PGE), because no sulfide in the mantle holds PGE in
568 the source and most PGE will dissolve into the magma. When such relatively oxidizing
569 magma arrives at the shallow magma chamber, more reduced conditions are required
570 to segregate sulfide rather than sulfate from the magma. This scenario was postulated
571 by Deng et al. (2014) and Zhao et al. (2016), who proposed that graphite assimilation
572 may play a critical role in causing sulfide segregation in the Ni–Cu deposits in NW
573 China. However, there is no reason to invoke an extremely high fO_2 (> QFM +2) for the
574 mantle source as well as the primary magma of the Permian deposits. Partial melting of
575 such source would generate PGE rich magmas, but no sign of PGE rich magma has
576 been observed in these deposits; the opposite is true in that the host magmas to all the
577 intrusions appear to be PGE depleted (Li et al., 2012; Zhang et al., 2011; Mao et al.,
578 2014a; Xue et al., 2016). Moreover, even in the Poyi intrusion, which was formed by

579 the most oxidized magma of the deposits in NW China, the oxygen fugacity is still
580 within the range where most of the S is dissolved as sulfide rather than sulfate. The
581 reduction accompanying the differentiation of the parental magma (Fig.14) does not
582 seem to be due to fractional crystallization and therefore suggests the assimilation of
583 graphite and sulfur bearing crustal material that also introduced the extra S to trigger
584 sulfide saturation.

585 *Origin of the variation in Ni tenor in sulfide*

586 The Ni content and the Fo value in olivine are related to Ni content and Mg/Fe
587 values in the magma from which the olivines are crystallized by partition coefficients,
588 which have been experimentally determined (Kiseeva and Wood 2013; Naldrett 2004;
589 Roeder and Emslie 1970) and therefore can be used to infer composition of the magma.
590 The spread of Fo values in olivine from the Ni–Cu deposits in NW China (Fig. 9)
591 illustrates that these deposits are associated with magmas containing different Fe/Mg
592 ratios and Ni contents, which are consistent with the previous estimation of host magma
593 compositions using Fe/Mg equilibrium between olivine and silicate liquid (Li et al.
594 2012; Mao et al. 2014a; Mao et al. 2016; Xue et al. 2016).

595 On the basis that these Permian deposits in the east Tianshan were emplaced in a
596 similar crustal architecture and derived from the similar mantle source, probably
597 relating to the same event (Qin et al. 2011; Song et al. 2013; Su et al. 2011), we treat
598 the host magma of the Poyi intrusion, which has the highest Fo value in olivine and has

599 experienced only weak crustal contamination (Yang et al. 2014), as the parental magma
600 to model its fractionation process. In our modeling, olivine composition is calculated at
601 each step using the well-established Roeder and Emslie (1970) relationship for the
602 Mg/Fe K_D between olivine and silicate melt ($K_D = (FeO/MgO)_{Olivine}/(FeO/MgO)_{Liquid}$
603 =0.3). The residual magma compositions were estimated by subtracting the component
604 in olivine from the parental magma. The Ni content in the residual melt is calculated
605 from the Rayleigh fractional crystallization equation and the partitioning value of Ni
606 between less fractionated olivine (Fo>80) and magma ($D_{ol–magma}$) was estimated using
607 the composition based equation of Li and Ripley (2010) (Table 7). The partitioning
608 values of Ni between olivine and magma for the highly fractionated olivines were
609 assumed as 13 for olivine of Fo_{78} and 17 for olivine of Fo_{74} (See summary in Li and
610 Ripley, 2010). The olivine crystallized from more reducing magma will have higher
611 fayalite during reduce Fe^{3+} to Fe^{2+}, MELTS modeling indicates that change of one log
612 unit oxidation state of the magma will cause ~2 mol.% variation of Fo value in olivine,
613 which is easily within the range of variability that would be expected from trapped
614 liquid reactions (30% trapped liquid, Fig. 9b) (Barnes 1986). Thus, the oxygen fugacity
615 of the parental magma and the residual melts during fractionation were set as QFM +1
616 for simplicity. The olivine composition of most of the Ni–Cu deposits plots along the
617 olivine fractionation model line (Fig. 9), demonstrating their host magmas were formed
618 by a variable degree of olivine fractionation in depth by the parental magma. The
619 relative low Ni content in olivine recorded by the Hulu, Huangshanxi, and Tianyu

620 deposits could be the result of sulfide segregation along with olivine fractionation at
621 depth. The olivine compositions of the Kalatongke deposit in the East Junggar was also
622 plotted for comparison, although it is most likely belonged to a different system and
623 could derive from a different parental magma. Olivine composition from the
624 Kalatongke deposit are all plotted above the modelling line, also away from the trend
625 for the trapped liquid effect (Fig. 9b), but can be the result of olivine fractionation at
626 the beginning (0–15%) plus subsequent olivine+clinopyroxene+plagioclase
627 fractionation at 5:4:1 (Fig. 9b). Since Ni is compatible and Cu is incompatible in olivine,
628 olivine fractionation of the parental magma decreases the Ni content and increase the
629 Cu/Ni ratio in the evolved magmas; thus sulfides segregated from the more fractionated
630 magma will be depleted in Ni and enriched in Cu/Ni ratio relative to these segregated
631 from the less fractionated parental magmas. The observations that Ni tenor in sulfide
632 decreases with Fo value in olivine (Fig. 10) and Cu/Ni ratio in sulfide increases with
633 decrease of Fo value in olivine (Fig. 11c) are consistent with an interpretation that
634 sulfides from the Ni–Cu deposits in NW China were segregated from similar parental
635 magmas that have experienced variable degree of olivine fractionation. R-factor model
636 using the Ni concentration in the residual silicate melts and calculated D_{Ni} between
637 sulfide and silicate from the equation of Kiseeva and Wood (2013), indicates that these
638 sulfides were segregated from variable R value, varying from 300 to 7000 (Fig. 10,
639 Table 7). The Poyi deposit is characterized by high R value (1000-7000), which is
640 significantly higher than other deposits (200-3000). The enrichment of Ni tenor in

641 sulfide of the Huangshannan and Tulaergen deposits relative to other Ni–Cu deposits
642 with similar Fo value in olivine (Fig. 10) may be the result of extra Ni sequestered from
643 olivine via open–system olivine–sulfide–silicate melt equilibrium (Fig. 9a) (Barnes et
644 al. 2013; Mao et al. 2017). In summary, the variation in Ni tenor in sulfides from the
645 east Tianshan Ni–Cu deposits is controlled by variable R-values and host magma
646 compositions that have been derived from the various degree of olivine fractionation
647 before the final emplacement. Relatively high Ni tenor in sulfide may be a consequence
648 of equilibration with olivine-phyric magmas.

649 *A genetic model for the Ni–Cu deposits in NW China*

650 A genetic model of the Permian Ni–Cu deposits in east Tianshan is illustrated in
651 Fig. 15. The low and variable degree of partial melting of supra-subduction zone mantle
652 gave rise to the primary magmas, which have high Ni and relatively low PGE
653 concentrations. After (5–10 %) olivine fractionation during ascent, the mafic magmas
654 entrained immiscible sulfide due to sulfide assimilation in the crust (Mao et al. 2016;
655 Xia et al. 2013; Xue et al. 2016; Yang et al. 2014). These sulfide-loaded melts got
656 emplaced into dike and dike–keel like structural traps, in which sulfides interacted with
657 a variable amount of silicate melts, giving rise to high Ni and relatively high PGE tenor
658 sulfides, such as the Huangshannan and Poyi deposits (Fig. 15a). These magmas had
659 relatively high oxygen fugacity (~QFM +1), reflecting a supra-subduction zone mantle
660 source and implying limited interaction with reduced country rocks. Some of the

mantle–derived magmas experienced a larger amount of olivine fractionation (15–20%) at depth, reducing the Ni concentration but without greatly changing the PGE concentrations, giving rise to magmas with decreased Ni contents. Meanwhile, the differentiated magma becoming increasingly reduced due to contamination with reduced (presumably graphite) country rocks, during which immiscible sulfide segregated from the magma and became entrained in the magma flow. These sulfide-loaded magmas gave rise to deposits with reduced Ni tenors and relatively reducing oxidation state ($-2 < \Delta QFM < 0$) in the form of conduits, sills, and chonoliths (Fig. 15b). These moderate Ni tenor deposits comprise the Huangshandong, Huangshanxi, Xiangshanzhong, Tudun, and Tulaergen deposits.

The Kalatongke deposit in the East Junggar probably belongs to a different system compared to the Ni–Cu deposits occur in the east Tianshan. The relatively oxidizing nature of the Kalationgke magma, together with the wide presence of graphite-bearing wall rock and a high degree of crustal contamination, suggests that the parental magma, probably as well as its mantle source, are even more oxidized. The low Ni tenor in sulfide could be the result of significant olivine fractionation during ascent. Significant fractionation (>20 %, olivine, clinopyroxene, and plagioclase) of the mantle melts without substantially reducing material addition generated mildly oxidized magmas (~QFM +1) containing relatively low Ni concentrations and high Cu/Ni ratios. Emplacement of these evolved magmas formed the Kalatongke deposit (Fig. 15c) which has the highest Cu tenor and lowest Ni tenor among the Ni–Cu deposits in NW

682 China. Subsequently, significant MSS fractionation during sulfide percolation or
683 backward flow (Barnes et al. 2016) gave rise to the sulfides with variable Ni, Cu and
684 PGE tenors in the Kalatongke and Huangshandong mafic unit (Mao et al. 2015; Qian
685 et al. 2009; Song and Li 2009).
686

687 **Conclusions**

688 The exchange of Fe and Ni between coexisting olivine and sulfide liquid (KD)
689 serves as a monitor of oxygen fugacity, which can be estimated from the recalibrated
690 equation in this study. The calculated oxygen fugacity values of the Permian Ni–Cu
691 deposits in the CAOB, varying from QFM − 2 to ~QFM + 1, could be the result of the
692 progressive interaction of originally mildly oxidized magmas with reducing crustal
693 agents. Desktop microbeam XRF scanning is a useful tool to estimate the 100% sulfide
694 composition for magmatic Ni–Cu deposits, especially for samples with low Ni grade
695 and a high proportion of background Ni. The Permian Ni–Cu deposits in the CAOB
696 exhibit a wide range of Ni content in sulfide varying from ~3 to 16 wt% at the deposit
697 scale. The variation in Ni tenor in sulfide of these deposits is the result of sulfide
698 segregation from magmas with variable Ni contents. The magmatic Ni–Cu system in
699 the East Tianshan was formed by host magmas that experienced a variable amount of
700 olivine fractionation associated with assimilation of reduced country rock at depth. The
701 Kalatongke deposit in the East Junggar with low Ni content in sulfide (< 5 wt%) and
702 high Cu/Ni ratio was formed by a host magma that experienced significant pre

emplacement olivine fractionation. Fractional crystallization and crustal assimilation played important roles in giving rise to the variability of Ni content in sulfide and oxygen fugacity in the Ni–Cu deposits in the CAOB.

Acknowledgements

This study has been financially supported by grants from the National Key Research and Development Program of China (2017YFC0601204), the National Natural Science Foundation of China (41502095), the French agency for research (ANR project #12JS06-0009-01), and China Postdoctoral Science Foundation (2015M570146 Ya–Jing Mao). Xinjiang Nonferrous Metal Industry Group Ltd. is thanked for access to the Ni–Cu deposits in NW China. Xue–Jun Yan, Jun–Hui Xie, Yong Wang, Bin Wang, Guan–Liang Ren, Ding–Min Guo, and Yu–Zong Liang are thanked for their sharing of knowledge of the deposits in the field work. The assistance of Ida Di Carlo and Patricia Benoist-Julliot with the SEM and the electron microprobe in Orléans is acknowledged. Guohui Chen, Tongcheng Han, and Na Guo are acknowledged for their help on best-fit calibration for the experimental data. Ya–Jing Mao acknowledges the funding of the China Scholarship Council to support the visit to CSIRO as a postdoctoral fellow. SJB acknowledges support from the CSIRO Science Plus Science Leader program. Valuable comments from Margaux Le Vaillant, Sheng-Hong Yang, and Chusi Li improved the manuscript. Editors Wolfgang Maier and Bernd Lehmann are acknowledged for their helpful suggestions and editorial handling.

References

Asimow PD, Ghiorso MS (1998) Algorithmic modifications extending MELTS to calculate subsolidus phase relations. Am Mineral 83:1127-1132

Barnes SJ (1986) The effect of trapped liquid crystallization on cumulus mineral compositions in layered intrusions. Contrib Mineral Petr 93:524-531 doi:10.1007/BF00371722

Barnes SJ, Naldrett AJ (1985) Geochemistry of the J-M (Howland) Reef of the Stillwater Complex, Minneapolis Adit area; I, Sulfide chemistry and sulfide-olivine equilibrium. Econ Geol 80:627-645 doi:10.2113/gsecongeo.80.3.627

Barnes SJ, Cruden AR, Arndt N, Saumur BM (2016) The mineral system approach applied to magmatic Ni–Cu–PGE sulphide deposits. Ore Geol Rev 76:296-316 doi:http://dx.doi.org/10.1016/j.oregeorev.2015.06.012

Barnes SJ, Godel B, Gürer D, Brenan JM, Robertson J, Paterson D (2013) Sulfide-Olivine Fe-Ni Exchange and the Origin of Anomalously Ni Rich Magmatic Sulfides. Econ Geol 108:1971-1982 doi:10.2113/econgeo.108.8.1971

Barnes SJ, Osborne GA, Cook D, Barnes L, Maier WD, Godel B (2011) The Santa Rita Nickel Sulfide Deposit in the Fazenda Mirabela Intrusion, Bahia, Brazil: Geology, Sulfide Geochemistry, and Genesis. Econ Geol 106:1083-1110 doi:10.2113/econgeo.106.7.1083

BGMRXUAR (Bureau of Geology and mineral Resources of Xinjiang Uygur Autonomous Region) (1993) Regional Geology of Xinjiang Uygur

745 Autonomous Region. Geological Publishing House, Beijing, 1-841
746 Botcharnikov R, Almeev R, Koepke J, Holtz F (2008) Phase relations and liquid lines
747 of descent in hydrous ferrobasalt—implications for the Skaergaard intrusion and
748 Columbia River flood basalts. J Petrol 49:1687-1727
749 Brenan JM (2003) Effects of fO2, fS2, temperature, and melt composition on Fe-Ni
750 exchange between olivine and sulfide liquid: implications for natural olivine–
751 sulfide assemblages. Geochim Cosmochim Ac 67:2663-2681
752 doi:10.1016/s0016-7037(02)01416-3
753 Brenan JM, Caciagli NC (2000) Fe–Ni exchange between olivine and sulphide liquid:
754 implications for oxygen barometry in sulphide-saturated magmas. Geochim
755 Cosmochim Ac 64:307-320 doi:http://dx.doi.org/10.1016/S0016-
756 7037(99)00278-1
757 Brenan JM, Li C (2000) Constraints on Oxygen Fugacity during Sulfide Segregation in
758 the Voisey's Bay Intrusion, Labrador, Canada. Econ Geol 95:901-915
759 doi:10.2113/gsecongeo.95.4.901
760 Chai F, Zhang Z, Mao J, Dong L, Zhang Z, Wu H (2008) Geology, petrology and
761 geochemistry of the Baishiquan Ni–Cu-bearing mafic–ultramafic intrusions in
762 Xinjiang, NW China: Implications for tectonics and genesis of ores. J Asian
763 Earth Sci 32:218-235 doi:http://dx.doi.org/10.1016/j.jseaes.2007.10.014
764 Deng Y-F, Song X-Y, Chen L-M et al. (2014) Geochemistry of the Huangshandong Ni–
765 Cu deposit in northwestern China: Implications for the formation of magmatic

766 sulfide mineralization in orogenic belts. Ore Geol Rev 56:181-198
767 doi:10.1016/j.oregeorev.2013.08.012
768 Deng Y-F, Song X-Y, Hollings P, Zhou T, Yuan F, Chen L-M, Zhang D (2015) Role of
769 asthenosphere and lithosphere in the genesis of the Early Permian Huangshan
770 mafic–ultramafic intrusion in the Northern Tianshan, NW China. Lithos
771 227:241-254 doi:http://dx.doi.org/10.1016/j.lithos.2015.04.014
772 Fleet ME, MacRae ND (1988) Partition of Ni between olivine and sulfide: equilibria
773 with sulfide-oxide liquids. Contrib Mineral Petr 100:462-469
774 doi:10.1007/bf00371375
775 Frost DJ, McCammon CA (2008) The Redox State of Earth's Mantle. Annual Review
776 of Earth and Planetary Sciences 36:389-420
777 doi:doi:10.1146/annurev.earth.36.031207.124322
778 Gaetani GA, Grove TL (1997) Partitioning of moderately siderophile elements among
779 olivine, silicate melt, and sulfide melt: constraints on core formation in the Earth
780 and Mars. Geochim Cosmochim Ac 61:1829-1846
781 Gao J-F, Zhou M-F (2013) Generation and evolution of siliceous high magnesium
782 basaltic magmas in the formation of the Permian Huangshandong intrusion
783 (Xinjiang, NW China). Lithos 162:128-139 doi:DOI
784 10.1016/j.lithos.2013.01.002
785 Gao JF, Zhou MF, Lightfoot PC, Wang CY, Qi L (2012) Origin of PGE-Poor and Cu-
786 Rich Magmatic Sulfides from the Kalatongke Deposit, Xinjiang, Northwest

China. Econ Geol 107:481-506 doi:10.2113/econgeo.107.3.481

Grinenko L (1985) Sources of sulfur of the nickeliferous and barren gabbro-dolerite intrusions of the northwest Siberian platform. Int Geol Rev 27:695-708

Han BF, Ji JQ, Song B, Chen LH, Li Z (2004) SHRIMP zircon U-Pb ages of kalatongke No. 1 and Huangshandong Cu-Ni-bearing mafic-ultramafic complexes, North Xinjiang, and geological implications. Chinese Sci Bull 49:2424-2429 doi:Doi 10.1360/04wd0163

Han CM, Xiao WJ, Zhao GC, Ao SJ, Zhang JE, Qu WJ, Du AD (2010) In-situ U-Pb, Hf and Re-Os isotopic analyses of the Xiangshan Ni-Cu-Co deposit in Eastern Tianshan (Xinjiang), Central Asia Orogenic Belt Constraints on the timing and genesis of the mineralization. Lithos 120:547-562 doi:DOI 10.1016/j.lithos.2010.09.019

Han C, Xiao W, Zhao G et al. (2013) SIMS U-Pb zircon dating and Re-Os isotopic analysis of the Hulu Cu-Ni deposit, eastern Tianshan, Central Asian Orogenic Belt, and its geological significance. Journal of Geosciences 58:251-270

Iacono-Marziano G, Gaillard F, Scaillet B, Polozov AG, Marecal V, Pirre M, Arndt NT (2012) Extremely reducing conditions reached during basaltic intrusion in organic matter-bearing sediments. Earth Planet Sc Lett 357–358:319-326 doi:http://dx.doi.org/10.1016/j.epsl.2012.09.052

Jahn BM (2004) The central Asian orogenic belt and growth of the continental crust in the phanerozoic. Geol Soc Spec Publ 226:73-100 doi:Doi

10.1144/Gsl.Sp.2004.226.01.05

Jugo PJ (2009) Sulfur content at sulfide saturation in oxidized magmas. Geology 37:415-418 doi:10.1130/g25527a.1

Kiseeva ES, Wood BJ (2013) A simple model for chalcophile element partitioning between sulphide and silicate liquids with geochemical applications. Earth Planet Sc Lett 383:68-81 doi:http://dx.doi.org/10.1016/j.epsl.2013.09.034

Li C, Ripley EM (2010) The relative effects of composition and temperature on olivine-liquid Ni partitioning: Statistical deconvolution and implications for petrologic modeling. Chem Geol 275:99-104 doi:http://dx.doi.org/10.1016/j.chemgeo.2010.05.001

Li C, Ripley EM, Naldrett AJ (2003) Compositional variations of olivine and sulfur isotopes in the Noril'sk and Talnakh intrusions, Siberia: Implications for ore-forming processes in dynamic magma conduits. Econ Geol Bull Soc 98:69-86

Li C, Zhang M, Fu P, Qian ZZ, Hu P, Ripley EM (2012) The Kalatongke magmatic Ni-Cu deposits in the Central Asian Orogenic Belt, NW China: product of slab window magmatism? Miner Deposita 47:51-67 doi:DOI 10.1007/s00126-011-0354-7

Li C, Zhang Z, Li W, Wang Y, Sun T, Ripley EM (2015) Geochronology, petrology and Hf–S isotope geochemistry of the newly-discovered Xiarihamu magmatic Ni–Cu sulfide deposit in the Qinghai–Tibet plateau, western China. Lithos 216–217:224-240 doi:http://dx.doi.org/10.1016/j.lithos.2015.01.003

829 Li X, Wang D, Zhao S (2014) The Discovery of Baixintan Magmatic Ni-Cu Sulfide
830 Deposits in Hami Area, Xinjiang. Xinjiang Geology 32:466-469
831 Lightfoot PC, Evans-Lamswood D (2015) Structural controls on the primary
832 distribution of mafic–ultramafic intrusions containing Ni–Cu–Co–(PGE)
833 sulfide mineralization in the roots of large igneous provinces. Ore Geol Rev
834 64:354-386 doi:http://dx.doi.org/10.1016/j.oregeorev.2014.07.010
835 Maier W, Groves D (2011) Temporal and spatial controls on the formation of magmatic
836 PGE and Ni–Cu deposits. Miner Deposita 46:841-857 doi:10.1007/s00126-011-
837 0339-6
838 Maier WD, Smithies RH, Spaggiari CV et al. (2016) Petrogenesis and Ni-Cu sulphide
839 potential of mafic-ultramafic rocks in the Mesoproterozoic Fraser Zone within
840 the Albany-Fraser Orogen, Western Australia. Precambrian Res
841 doi:http://dx.doi.org/10.1016/j.precamres.2016.05.004
842 Mao JW, Pirajno F, Zhang ZH et al. (2008) A review of the Cu-Ni sulphide deposits in
843 the Chinese Tianshan and Altay orogens (Xinjiang Autonomous Region, NW
844 China): Principal characteristics and ore-forming processes. J Asian Earth Sci
845 32:184-203 doi:10.1016/j.jseaes.2007.10.006
846 Mao Y-J, Qin K-Z, Li C, Xue SC, Ripley EM (2014a) Petrogenesis and ore genesis of
847 the Permian Huangshanxi sulfide ore-bearing mafic-ultramafic intrusion in the
848 Central Asian Orogenic Belt, western China. Lithos 200:111-125 doi:DOI
849 10.1016/j.lithos.2014.04.008

Mao Y-J, Qin K-Z, Tang D, Xue S-C, Tian Y, Feng H (2014b) Multiple phases of magma emplacement and mineralization of eastern Tianshan, Xinjiang: Examplified by Huangshan Ni-Cu deposit. Acta Petrol Sin 30:1575-1594

Mao Y-J, Qin K-Z, Li C, Tang D-M (2015) A modified genetic model for the Huangshandong magmatic sulfide deposit in the Central Asian Orogenic Belt, Xinjiang, western China. Miner Deposita 50:65-82 doi:10.1007/s00126-014-0524-5

Mao Y-J, Qin K-Z, Tang D-M, Feng H-Y, Xue S-C (2016) Crustal contamination and sulfide immiscibility history of the Permian Huangshannan magmatic Ni-Cu sulfide deposit, East Tianshan, NW China. J Asian Earth Sci 129:22-37 doi:http://dx.doi.org/10.1016/j.jseaes.2016.07.028

Mao Y-J, Qin K-Z, Barnes SJ, Tang D-M, Xue S-C, Le Vaillant M (2017) Genesis of the Huangshannan high-Ni tenor magmatic sulfide deposit in the Eastern Tianshan, northwest China: Constraints from PGE geochemistry and Os–S isotopes. Ore Geol Rev doi:http://dx.doi.org/10.1016/j.oregeorev.2017.05.015

Mungall JE, Brenan JM (2014) Partitioning of platinum-group elements and Au between sulfide liquid and basalt and the origins of mantle-crust fractionation of the chalcophile elements. Geochim Cosmochim Ac 125:265-289 doi:http://dx.doi.org/10.1016/j.gca.2013.10.002

Naldrett AJ (2004) Magmatic Sulfide Deposits: Geology, Geochemistry and Exploration. Springer: 1-727

871 Parkinson IJ, Arculus RJ (1999) The redox state of subduction zones: insights from arc-
872 peridotites. Chem Geol 160:409-423
873 Qian ZZ, Wang JZ, Jiang CY, Jiao JG, Yan HQ, He K, Sun T (2009) Geochemistry
874 characters of platinum-group elements and its significances on the process of
875 mineralization in the Kalatongke Cu-Ni sulfide deposit, Xinjiang, China. Acta
876 Petrol Sin 25:832-844
877 Qin K-Z, Su B-X, Sakyi PA et al. (2011) Sims zircon U-Pb geochronology and Sr-Nd
878 isotopes of Ni-Cu-bearing mafic-ultramafic intrusions in Eastern tianshan and
879 Beishan in correlation with flood basalts in Tarim basin (NW china): Constraints
880 on a Ca. 280 Ma mantle plume. Am J Sci 311:237-260 doi:Doi
881 10.2475/03.2011.03
882 Qin K-Z, Tang D-M, Su B-X, Mao Y-J, Xue S-C (2012) The tectonic setting, style,
883 basic feature, relative erosion degree, ore-bearing evaluation sign, potential
884 analysis of mineralization of Cu-Ni bearing Permian mafic-ultramafic
885 complexes, Northern Xinjiang. Northwestern Geology 45:83-116
886 Roeder PL, Emslie RF (1970) Olivine-Liquid Equilibrium. Contrib Mineral Petr
887 29:275-289 doi:Doi 10.1007/Bf00371276
888 San J, Tian B, Lei J, Kang F, Qin K, Xu X (2003) A new discovery whole rocks
889 mineralized Cu: Ni sulfide deposit in Tulagen, Etat Tianshan, Xinjiang. Mineral
890 Deposits 22:270
891 Sciortino M, Mungall JE, Muinonen J (2015) Generation of High-Ni Sulfide and Alloy

892 Phases During Serpentinization of Dunite in the Dumont Sill, Quebec. Econ
893 Geol 110:733-761 doi:10.2113/econgeo.110.3.733
894 Song XY, Chen LM, Deng YF, Xie W (2013) Syncollisional tholeiitic magmatism
895 induced by asthenosphere upwelling owing to slab detachment at the southern
896 margin of the Central Asian Orogenic Belt. Journal of the Geological Society
897 170:941-950 doi:Doi 10.1144/Jgs2012-130
898 Song XY, Li XR (2009) Geochemistry of the Kalatongke Ni-Cu-(PGE) sulfide deposit,
899 NW China: implications for the formation of magmatic sulfide mineralization
900 in a postcollisional environment. Miner Deposita 44:303-327 doi:DOI
901 10.1007/s00126-008-0219-x
902 Su B-X, Qin K-Z, Sakyi PA et al. (2011) U–Pb ages and Hf–O isotopes of zircons from
903 Late Paleozoic mafic–ultramafic units in the southern Central Asian Orogenic
904 Belt: Tectonic implications and evidence for an Early-Permian mantle plume.
905 Gondwana Research 20:516-531 doi:10.1016/j.gr.2010.11.015
906 Su B-X, Qin K-Z, Tang D-M, Sakyi PA, Liu P-P, Sun H, Xiao Q-H (2013) Late
907 Paleozoic mafic–ultramafic intrusions in southern Central Asian Orogenic Belt
908 (NW China): Insight into magmatic Ni–Cu sulfide mineralization in orogenic
909 setting. Ore Geol Rev 51:57-73
910 doi:http://dx.doi.org/10.1016/j.oregeorev.2012.11.007
911 Sun H (2009) Ore-forming mechanism in conduit system and ore-bearing property
912 evaluation for mafic–ultramafic complex in Eastern Tianshan, Xinjiang.

913 Unpublished PhD thesis. Institute of Geology and Geophysics, Chinese
914 Academy of Sciences. p274
915 Sun T, Qian Z-Z, Li C, Xia M-Z, Yang S-H (2013a) Petrogenesis and economic
916 potential of the Erhongwa mafic–ultramafic intrusion in the Central Asian
917 Orogenic Belt, NW China: Constraints from olivine chemistry, U–Pb age and
918 Hf isotopes of zircons, and whole-rock Sr–Nd–Pb isotopes. Lithos 182-
919 183:185-199 doi:10.1016/j.lithos.2013.10.004
920 Sun T, Qian ZZ, Deng YF, Li CS, Song XY, Tang QY (2013b) PGE and Isotope (Hf-
921 Sr-Nd-Pb) Constraints on the Origin of the Huangshandong Magmatic Ni-Cu
922 Sulfide Deposit in the Central Asian Orogenic Belt, Northwestern China. Econ
923 Geol 108:1849-1864 doi:10.2113/econgeo.108.8.1849
924 Tang D, Qin K, Li C, Qi L, Su B, Qu W (2011) Zircon dating, Hf–Sr–Nd–Os isotopes
925 and PGE geochemistry of the Tianyu sulfide-bearing mafic–ultramafic intrusion
926 in the Central Asian Orogenic Belt, NW China. Lithos 126:84-98
927 doi:10.1016/j.lithos.2011.06.007
928 Tang D, Qin K, Su B et al. (2013) Magma source and tectonics of the Xiangshanzhong
929 mafic–ultramafic intrusion in the Central Asian Orogenic Belt, NW China,
930 traced from geochemical and isotopic signatures. Lithos 170–171:144-163
931 doi:http://dx.doi.org/10.1016/j.lithos.2013.02.013
932 Taylor JR, Wall VJ, Pownceby MI (1992) The calibration and application of accurate
933 redox sensors. Am Mineral 77:284-295

934 Tian W, Campbell IH, Allen CM et al. (2010) The Tarim picrite-basalt-rhyolite suite, a
935 Permian flood basalt from northwest China with contrasting rhyolites produced
936 by fractional crystallization and anatexis. Contrib Mineral Petr 160:407-425
937 doi:DOI 10.1007/s00410-009-0485-3
938 Wang RM, Zhao CL (1991) Kalatongke Cu-Ni Sulfide No. 1 Ore Deposit in Xinjiang.
939 Geological Publishing House, Beijing. 1-319
940 Wang RM, Liu DQ, Yin DT (1987) The conditions of controlling metallogny of Cu-Ni
941 sulfide ore deposits and the orientation of finding ore Hami, Xinjiang, China.
942 Journal of Mineralogy and Petrology 7:1-152
943 Wang Y, Zhang Z, You M, Li X, Li K, Wang B (2015) Chronological and gechemical
944 charcateristics of the Baixintan Ni-Cu deposit in Eastern Tianshan Mountains,
945 Xinjiang, and their implications for Ni-Cu mineralization. Geol China 42:452-
946 467
947 Xia M-Z, Jiang C-Y, Li C, Xia Z-D (2013) Characteristics of a Newly Discovered Ni-
948 Cu Sulfide Deposit Hosted in the Poyi Ultramafic Intrusion, Tarim Craton, NW
949 China. Econ Geol 108:1865-1878 doi:10.2113/econgeo.108.8.1865
950 Xiao WJ, Windley BF, Huang BC et al. (2009) End-Permian to mid-Triassic termination
951 of the accretionary processes of the southern Altaids: implications for the
952 geodynamic evolution, Phanerozoic continental growth, and metallogeny of
953 Central Asia. Int J Earth Sci (Geol Rundsch) 98:1189-1217 doi:DOI
954 10.1007/s00531-008-0407-z

955 Xue S, Qin K, Li C, Tang D, Mao Y, Qi L, Ripley EM (2016) Geochronological,
956 Petrological, and Geochemical Constraints on Ni-Cu Sulfide Mineralization in
957 the Poyi Ultramafic-Troctolitic Intrusion in the Northeast Rim of the Tarim
958 Craton, Western China. Econ Geol 111:1465-1484
959 doi:10.2113/econgeo.111.6.1465
960 Yang S-H, Zhou M-F, Lightfoot PC, Xu J-F, Wang CY, Jiang C-Y, Qu W-J (2014) Re–
961 Os isotope and platinum-group element geochemistry of the Pobei Ni–Cu
962 sulfide-bearing mafic‐ultramafic complex in the northeastern part of the Tarim
963 Craton. Miner Deposita 49:381-397 doi:10.1007/s00126-013-0496-x
964 Yang E (2015) Sediment environment and enrichment rule of ore-forming elements of
965 Lower Cambrian balck shale Series, Kuruktag-Beishan region, Xinjiang
966 Province. PhD thesis. China University of Geosciences, Wuhan, p 150
967 Zhang M, Li C, Fu P, Hu P, Ripley E (2011) The Permian Huangshanxi Cu–Ni deposit
968 in western China: intrusive–extrusive association, ore genesis, and exploration
969 implications. Miner Deposita 46:153-170 doi:10.1007/s00126-010-0318-3
970 Zhang ZC, Mao JW, Chai FM, Yan SH, Chen BL, Pirajno F (2009) Geochemistry of
971 the Permian Kalatongke Mafic Intrusions, Northern Xinjiang, Northwest China:
972 Implications for the Genesis of Magmatic Ni-Cu Sulfide Deposits. Econ Geol
973 104:185-203
974 Zhao Y, Xue C, Zhao X, Yang Y, Ke J (2015) Magmatic Cu–Ni sulfide mineralization
975 of the Huangshannan mafic–untramafic intrusion, Eastern Tianshan, China. J

976 Asian Earth Sci 105:155-172
977 doi:http://dx.doi.org/10.1016/j.jseaes.2015.03.031
978 Zhao Y, Xue C, Zhao X, Yang Y, Ke J, Zu B (2016) Variable mineralization processes
979 during the formation of the Permian Hulu Ni-Cu sulfide deposit, Xinjiang,
980 Northwestern China. J Asian Earth Sci 126:1-13
981 doi:http://dx.doi.org/10.1016/j.jseaes.2016.04.021
982 Zhou MF, Lesher CM, Yang ZX, Li JW, Sun M (2004) Geochemistry and petrogenesis
983 of 270 Ma Ni-Cu-(PGE) sulfide-bearing mafic intrusions in the Huangshan
984 district, Eastern Xinjiang, Northwest China: implications for the tectonic
985 evolution of the Central Asian orogenic belt. Chem Geol 209:233-257 doi:DOI
986 10.1016/j.chemgeo.2004.05.005

Figures

Fig. 1 Spatial distribution of magmatic Ni–Cu deposits in the CAOB (modified after Jahn, 2004, Li et al., 2012). Large circle represents Ni–Cu deposits contain Ni metal higher than 0.2 Mt, small circle represents Ni–Cu deposits contain less than 0.2 Mt Ni metal.

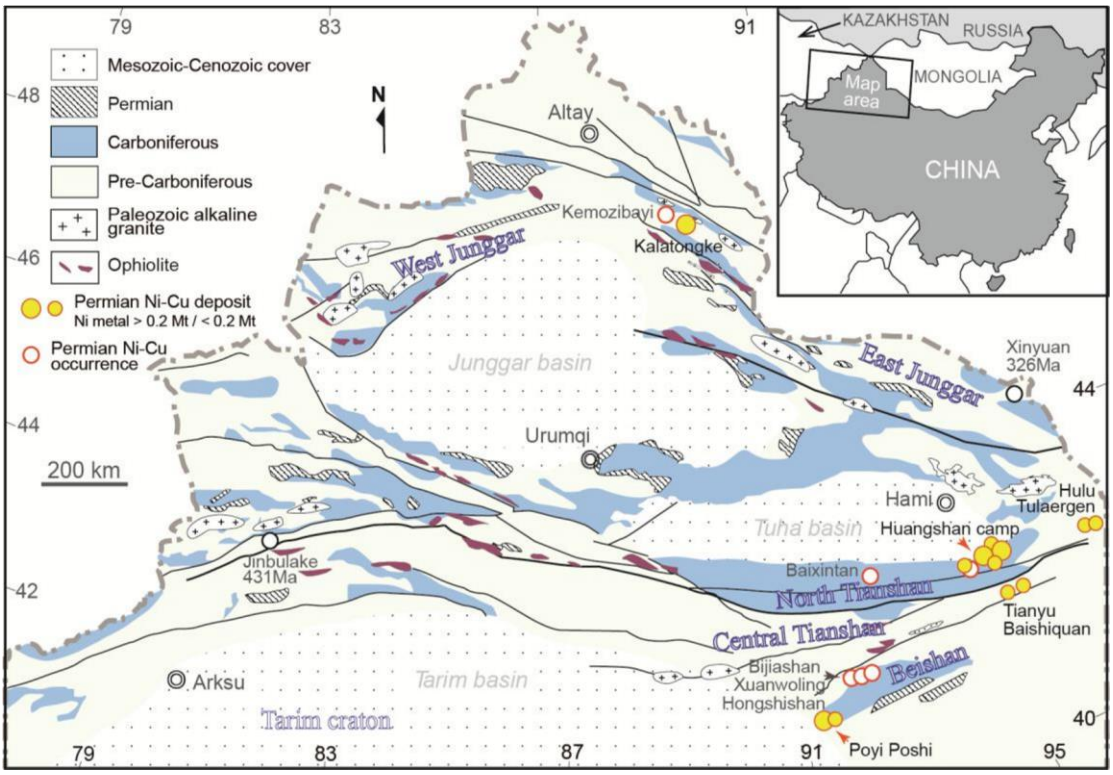

Fig. 2 A simplified geological map of the Xinjiang Uygur Autonomous region in NW China, showing the locality of the Permian mafic–ultramafic deposits/occurrences (modified from Mao et al., 2008). Magmatic Ni–Cu deposits within the Huangshan camp are composed of the Huangshanxi and Huangshandong deposits (> 0.2 Mt Ni metal), the Huangshannan, Xiangshanzhong, and Tudun deposits (< 0.2 Mt Ni metal), and the Erhongwa occurrence.

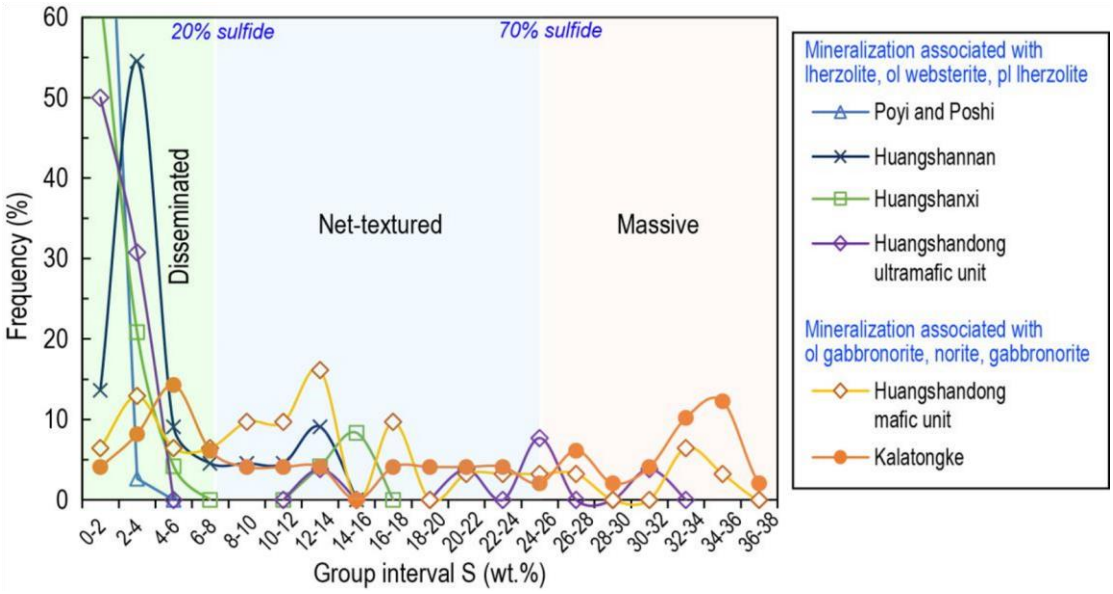

1004

1005 Fig. 3 Frequency distribution of S abundance in ores from the Ni–Cu deposits in

1006 the CAOB, illustrating the dominant sulfide texture for these deposits. Data source is

1007 listed in Table 1.

1008

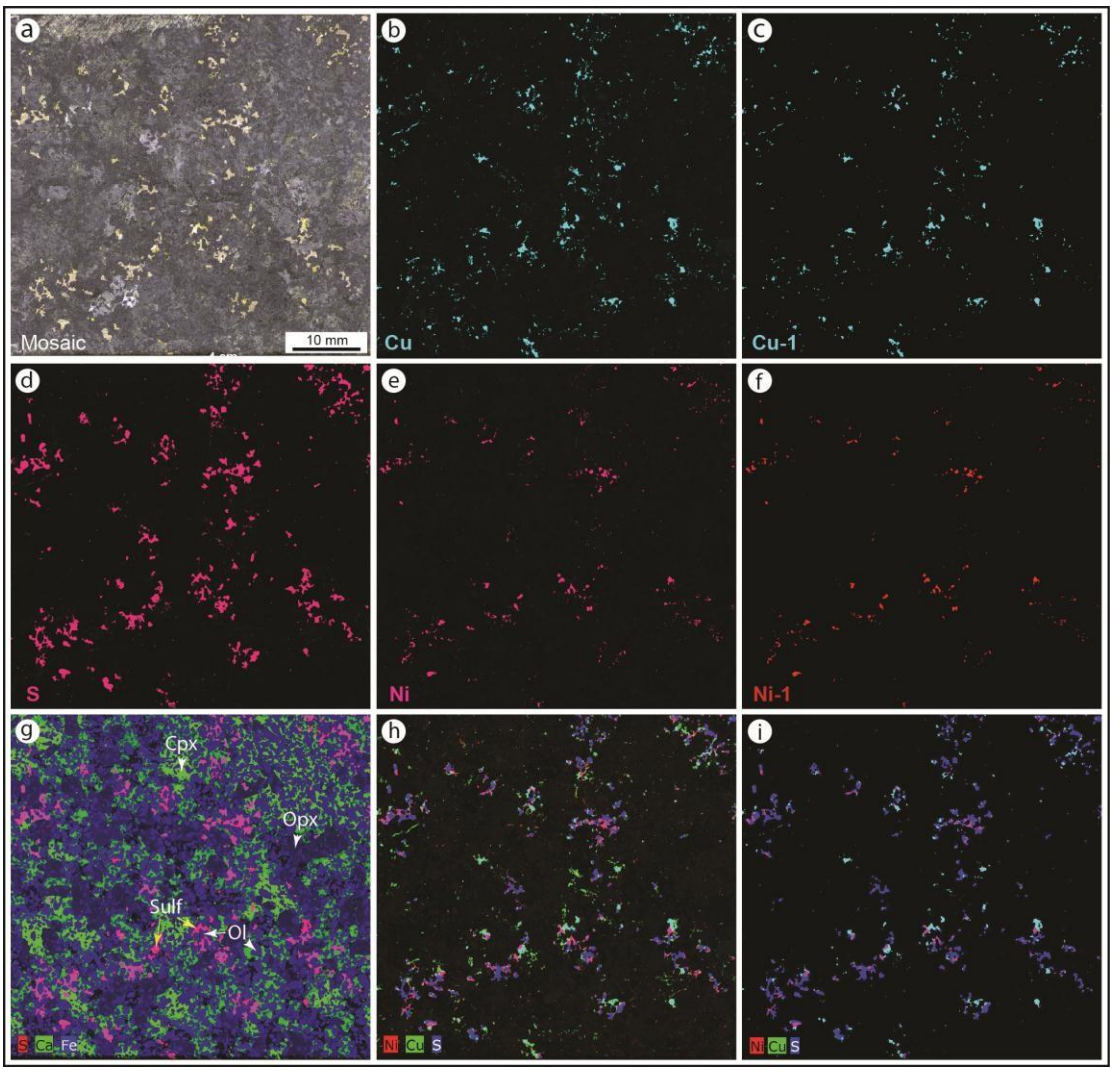

Fig. 4 Optical (a) and XRF images (b–i) of a disseminated lherzolite (06–04–711.5) from the Huangshanxi Ni–Cu deposit. (b), (d), and (e) are raw XRF images of Cu, S, and Ni from Tornado, whereas (c) and (f) are Cu and Ni images after processing; (g) is the combination of S in red, Ca in green, and Fe in blue images showing the distribution of sulfide, olivine, clinopyroxene, and orthopyroxene; (h) and (i) compare the raw XRF three element map (Ni-Cu-S) with the processed map.

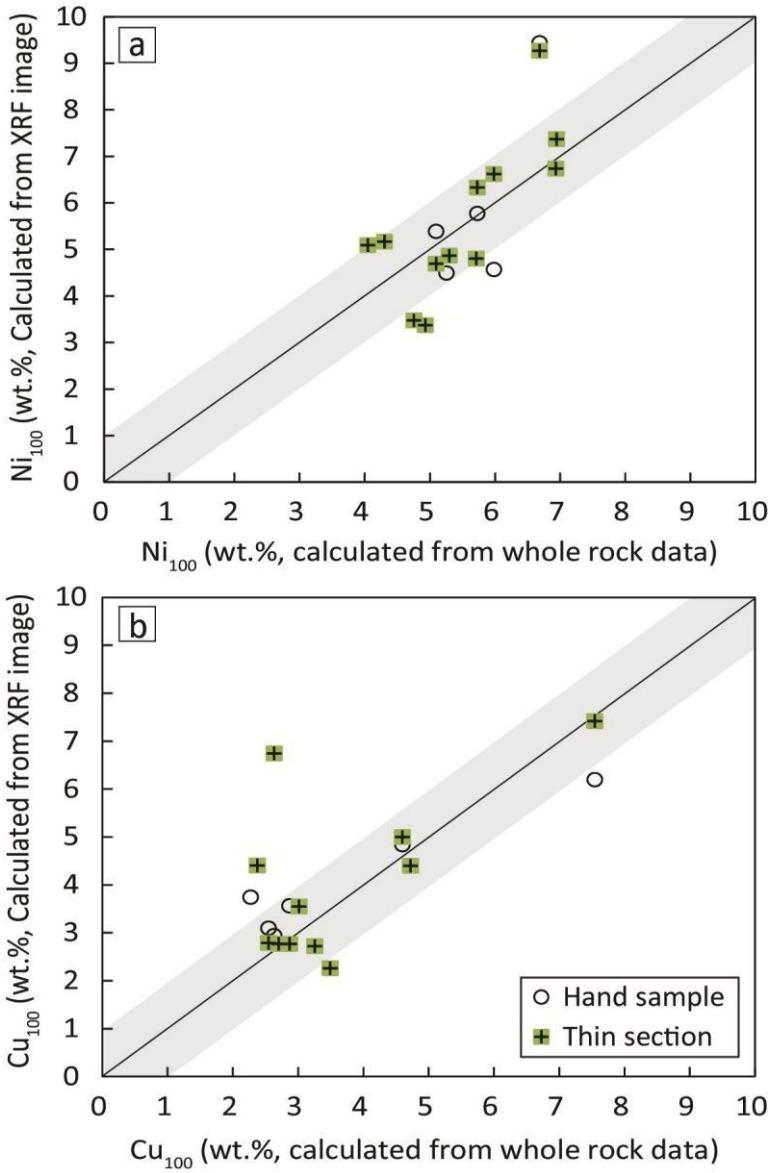

1019

1020 Fig. 5 Comparison between Ni tenors (a) and Cu tenors (b) calculated using whole

1021 rock S, Cu, Ni contents and these estimated by XRF images at both hand sample scale

1022 and thin section scale. Mineralized samples from the Huangshanxi (Mao et al., 2014)

1023 and Tudun (this study) Ni–Cu deposits are used for comparison.

1024

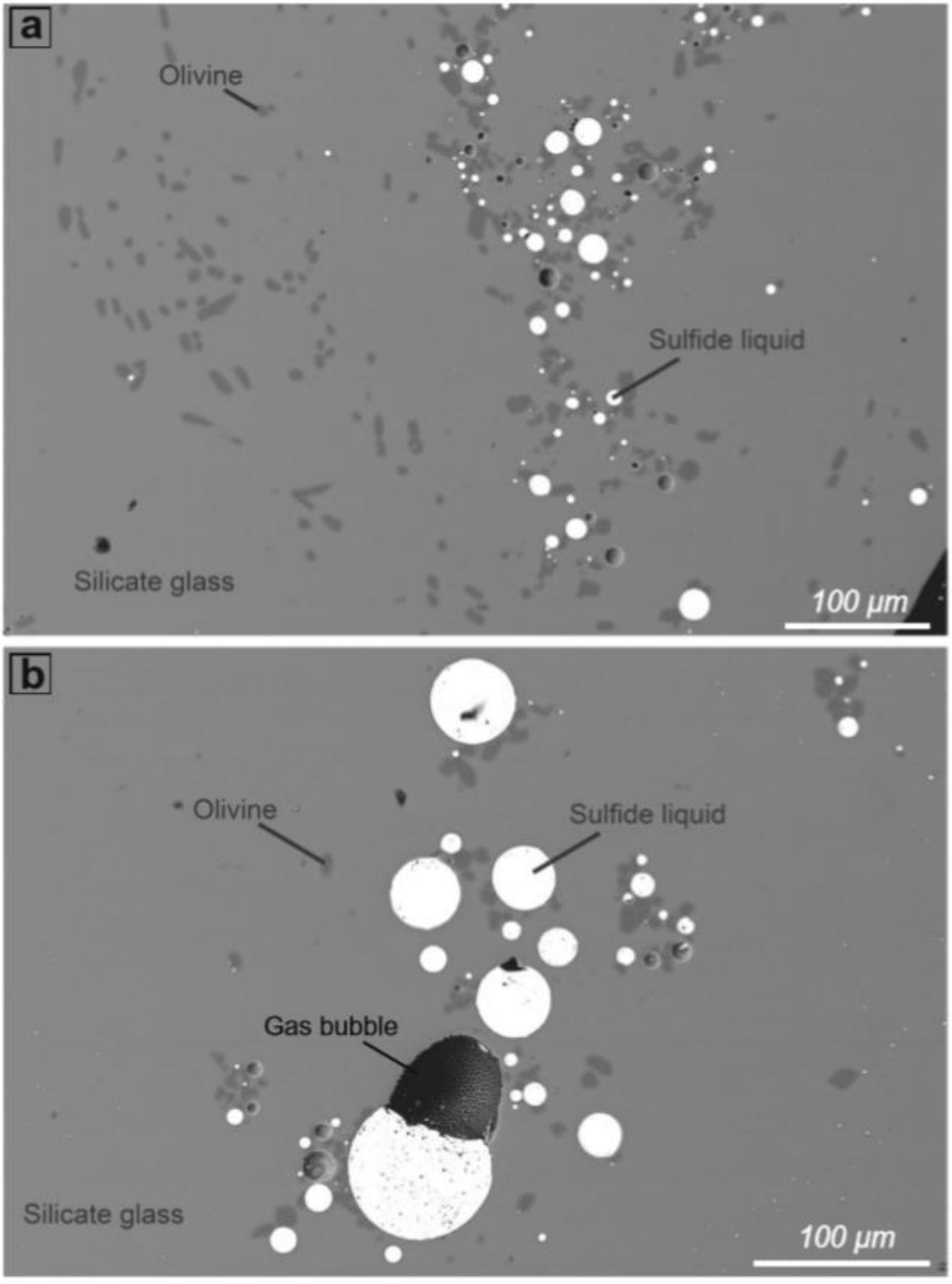

1025

1026 Fig. 6 Back-scattered electron images of a typical experimental product (sample
1027 GV159), showing the coexistence of silicate glass, sulfide droplets (with sensibly
1028 different sizes in a and b), olivine, and gas bubbles (b).

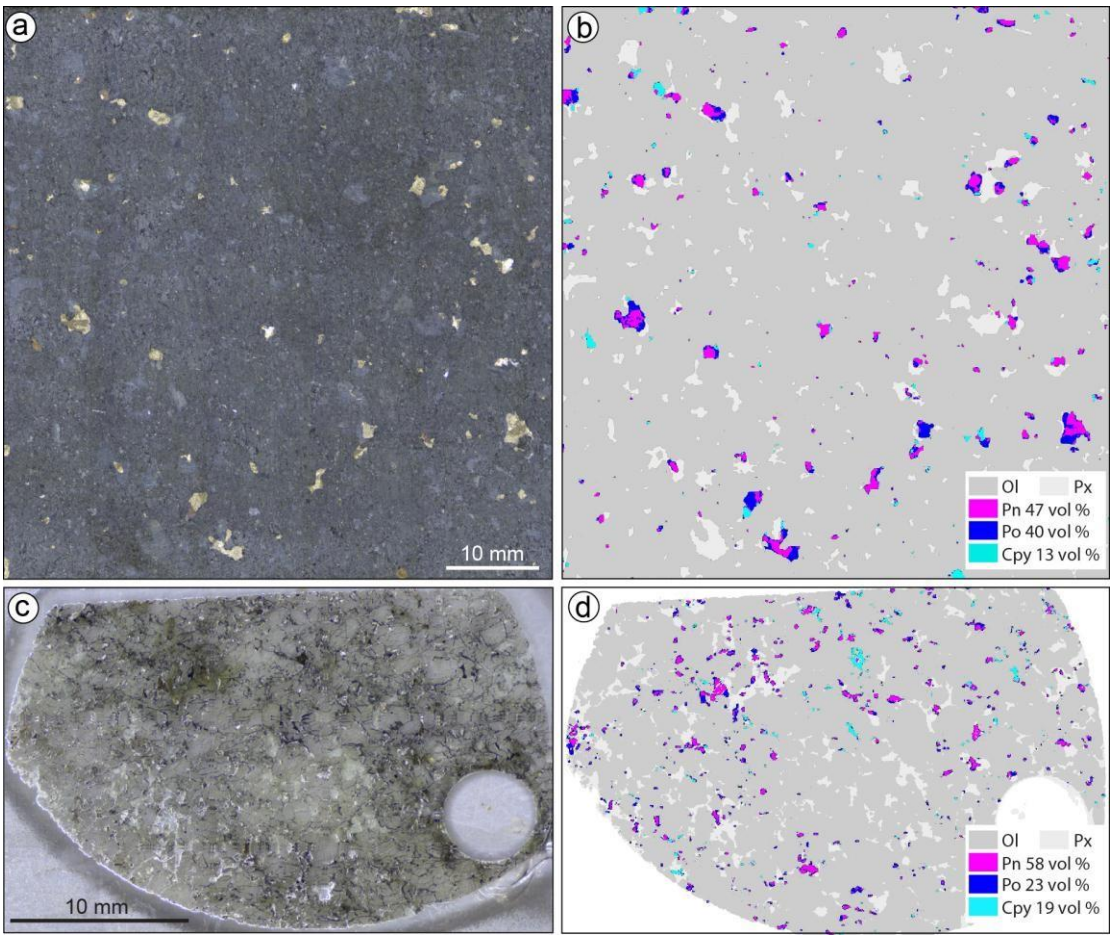

1029

1030 Fig. 8 Optical (a, c) and XRF image (b, d) of lherzolite from the Poyi deposit. The

1031 XRF image is shown as false–color showing the proportion of pentlandite, chalcopyrite,

1032 and pyrrhotite in 100% sulfide.

1033

1034

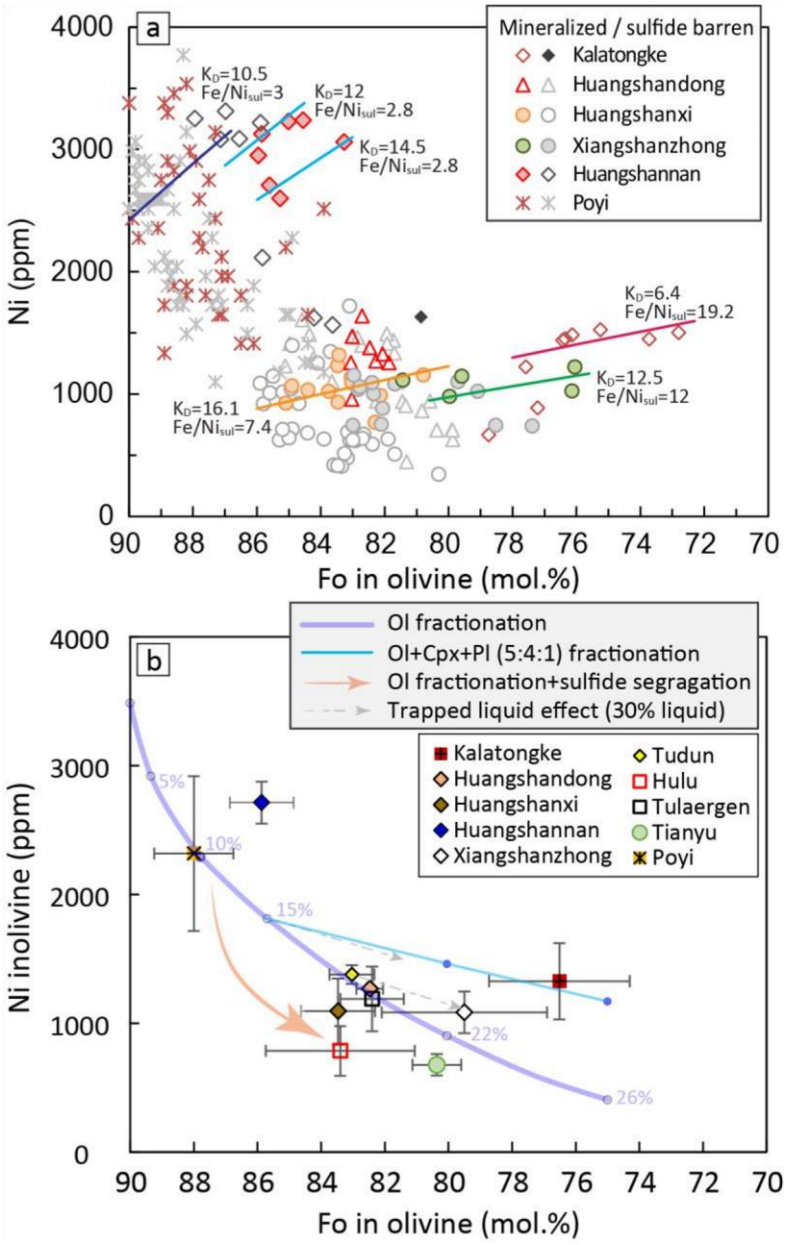

Fig. 9 Olivine compositional variation in Ni–Cu deposits in NW China. a Olivine compositional variation in samples from the Kalatongke, Huangshandong, Huangshanxi, Xiangshanzhong, Huangshannan, and Poyi deposits, illustrating negative correlations between Ni and Fo value which are derived from Fe/Ni exchange between olivine and sulfide. KD and Fe/Ni ratio in sulfide (Fe/Nisul) are listed in Tables 4 and 5. Other deposits are not plotted for clarity. b Average olivine composition for each deposit. Error bars are 2σ uncertainty. Data sources are listed in Table 1 and the parameters used in the model calculation are listed in Table 7. See text for the detailed explanation of the modeling lines.

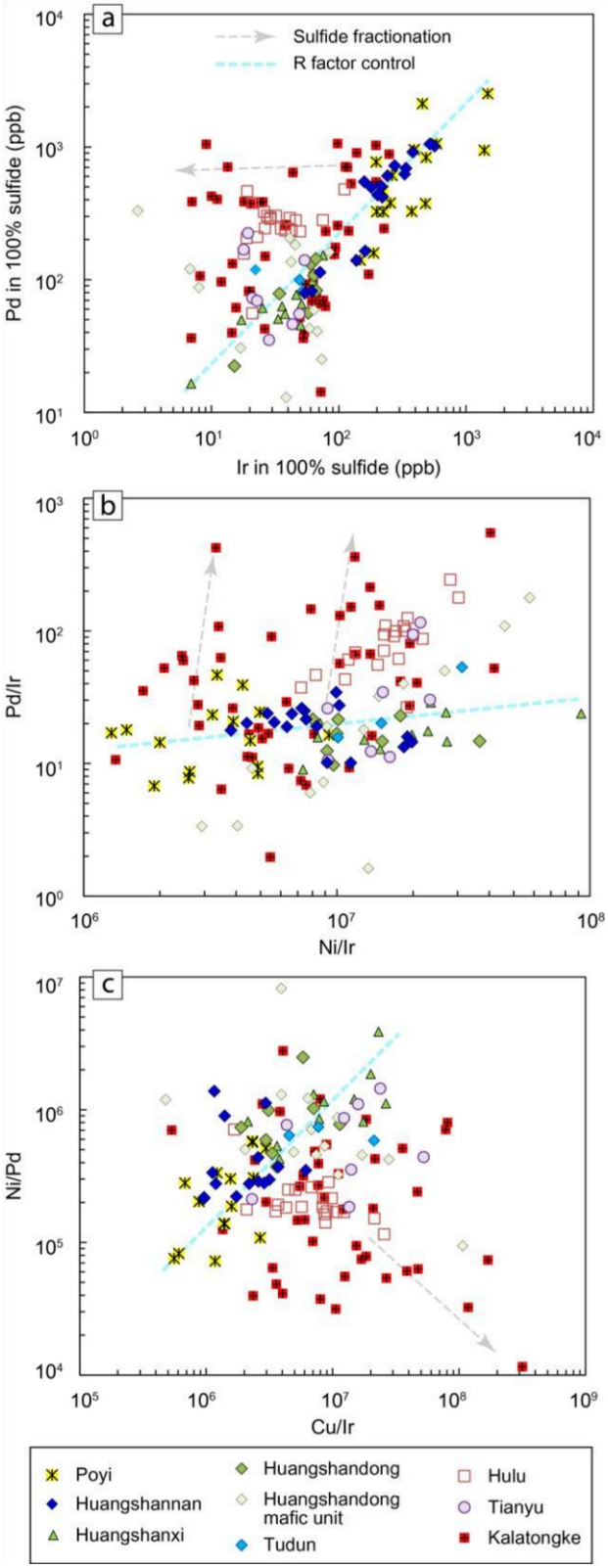

1045

1046 Fig. 5 Plots of Ir and Pd tenors (a) and Pd/Ir vs Ni/Ir ratios (b) and Ni/Pd vs Cu/Ir

1047 ratios (c) in sulfide from the Ni–Cu deposits in NW China.

1048

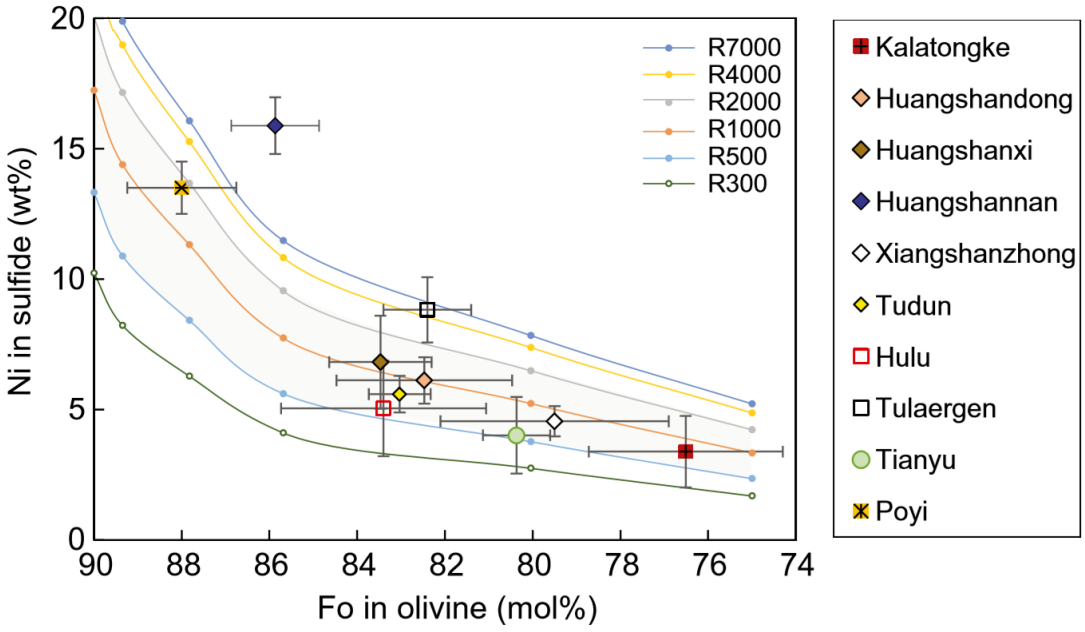

Fig.10 CorrelationbetweenFovalueinolivineandNitenorinsulfideof the Ni–Cu deposits in NW China. Error bars are 2σ uncertainty. The parameters used in the R value calculation are listed in Table 7. See text for the detailed explanation of the modeling lines.

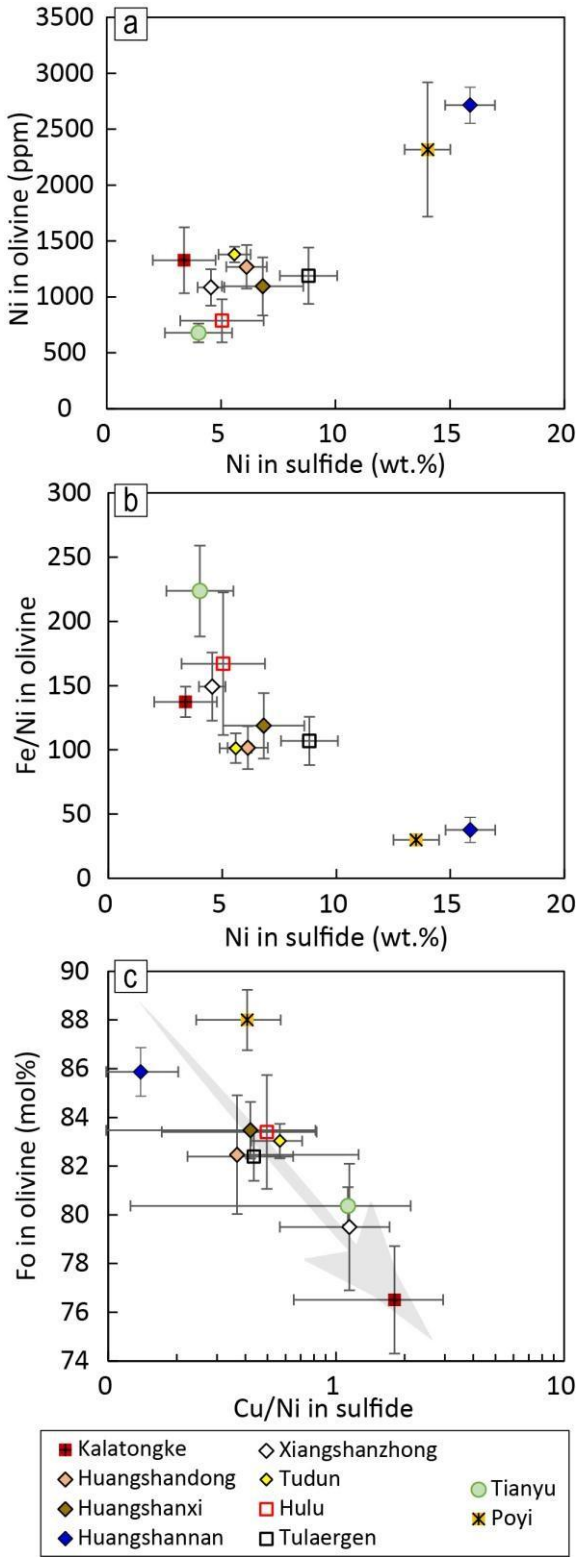

Fig. 11 Plots of Ni tenor in sulfide versus Ni content (a) and Fe/Ni ratio (b) inolivine, ccorrelationbetween Cu/Ni ratiosin sulfide andFovalues inolivine.GrayarrowsillustratethattheNitenorinsulfideincreaseswith the increase of Ni content in olivine (a) and with the decrease of Fe/Ni ratio in olivine (b), and Cu/Ni ratio in sulfide increases as Fo value in olivine decreases (c) for the Ni–Cu deposits in NW China. Error bars are 2σ uncertainty

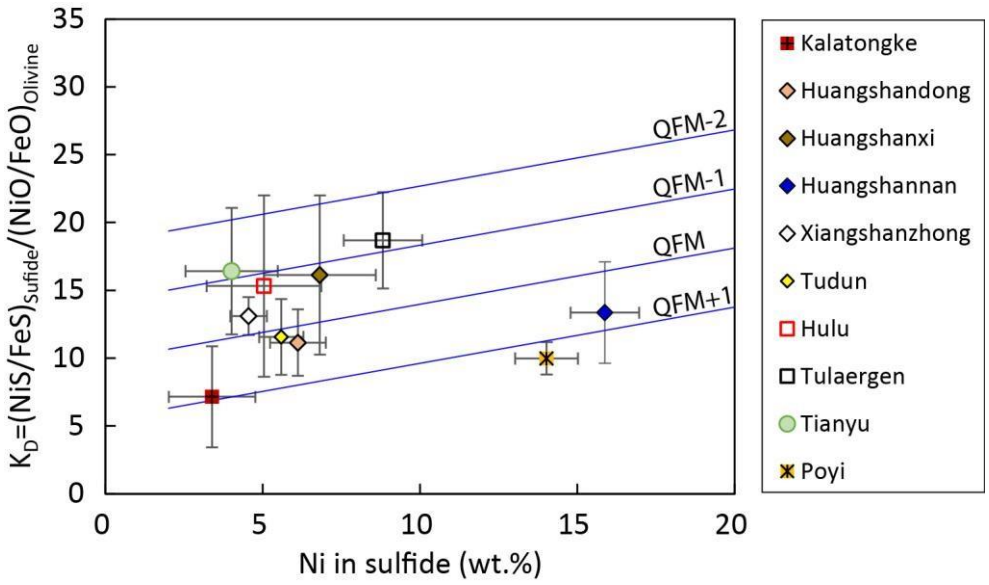

Fig. 12 Ni tenor in sulfide versus KD values. The baselines of oxygen fugacity were calculated using the recalibrated equation of this study. Error bars of the Tianyu and Hulu deposits are 2σ uncertainty. The error of KD in the individual sample is approximately ± 3.5

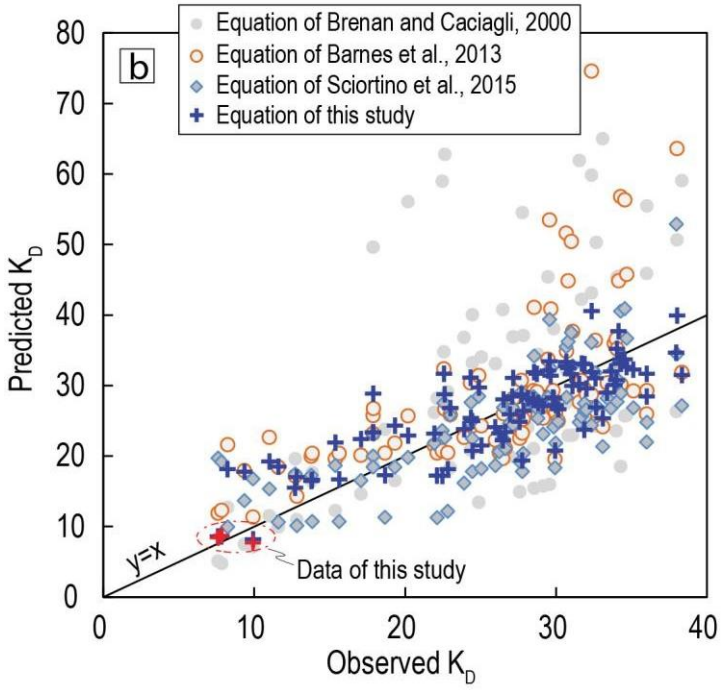

Fig. 13 Comparison of predicted KD and observed KD estimated by different equations. See Fig. 7 for the data source

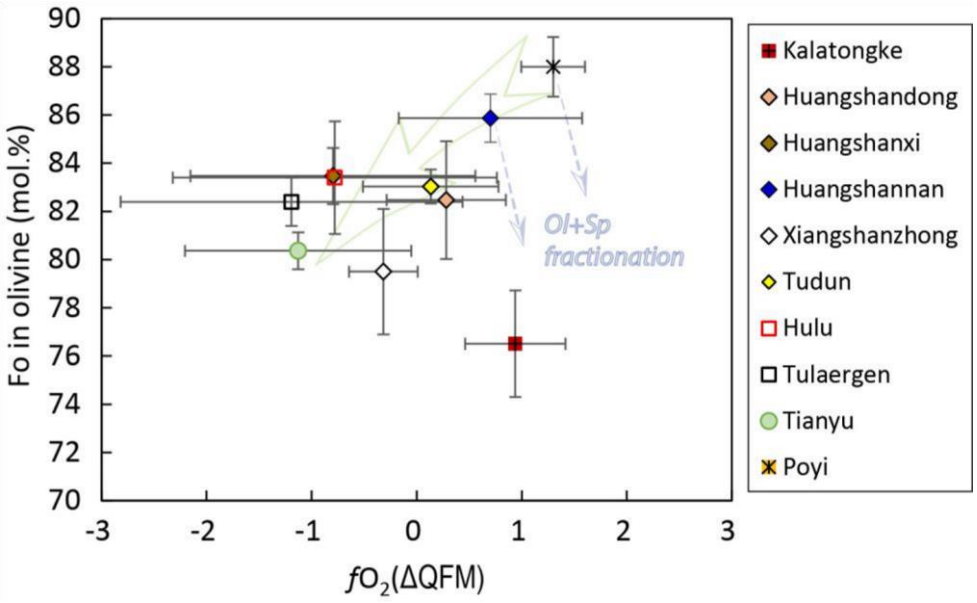

Fig. 14 Plot of oxygen fugacity shown as ΔQFM versus Fo values in olivinefortheNi–CudepositsinNWChina.Thegreenarrowshowsthat the oxidation state of the Ni–Cu deposits in the East Tianshan is becoming increasingly reduced as Fo value in olivine decreases; blue dashed lines illustrate the oxidation state of the Poyi and Huangshannan host magmas which slightly increases during olivine and spinel fractionation. Error bars of the Tianyu and Hulu deposits are 2σ uncertainty. The error of ΔQFM in the individual sample is approximately ± 0.8 log unit of ΔQFM

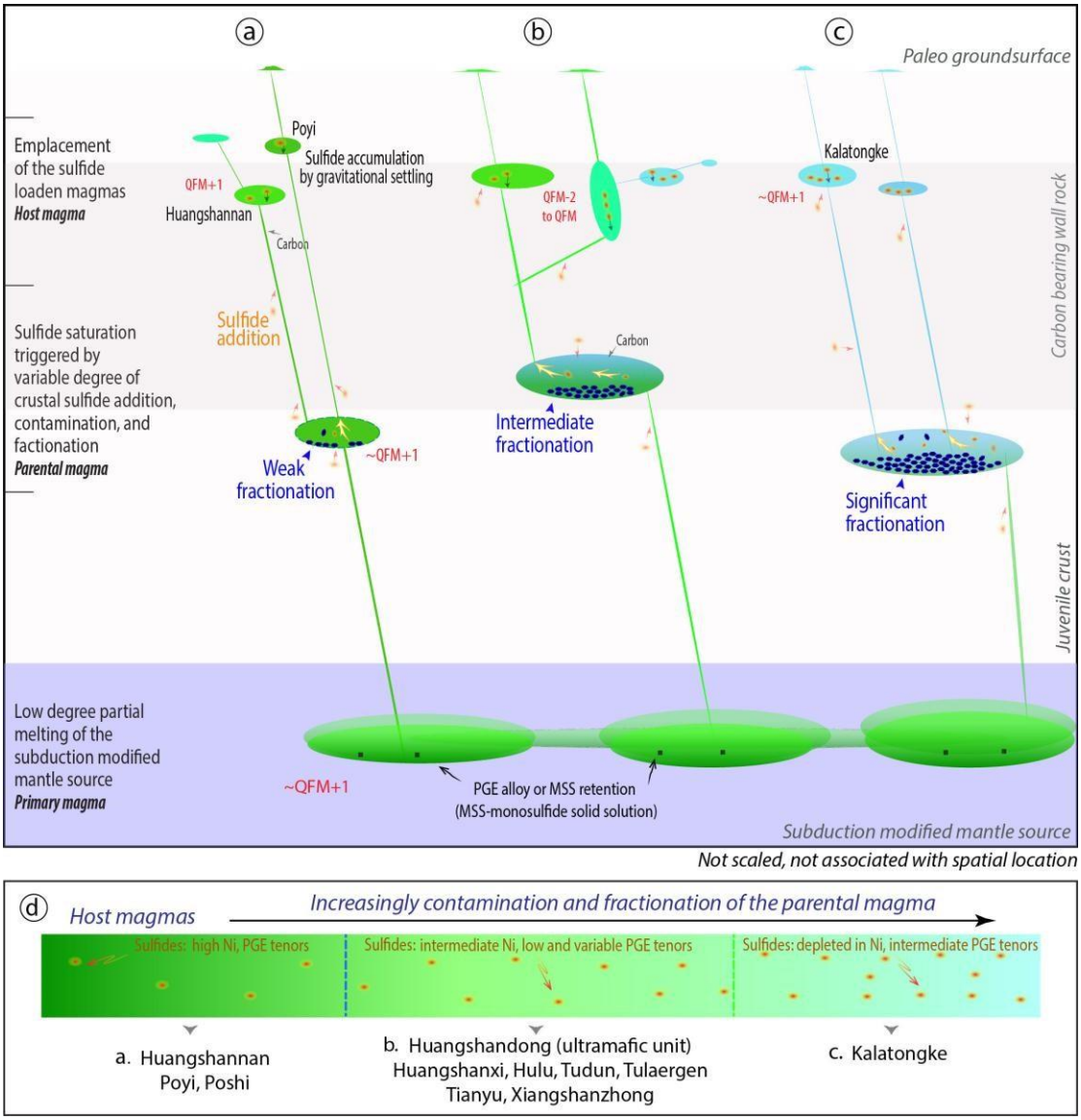

Fig. 15 A genetic model for the Ni–Cu deposits in NW China, showing the evolution of the Permian mantle partial melts in the continental crust (a-d). The relatively low degree of partial melting generated relatively oxidizing primary magma with substantial Ni and Cu but low PGE concentrations, leaving PGE alloy or sulfide in the mantle residue (a-c). Weak to significant fractionation and contamination by sulfide and reducing agents in the staging chamber or during ascent gave rise to magmas with variable oxygen fugacity (a-c) and Ni and Cu contents(d),whereasPGEconcentrationswerenotsignificantlymodified during magma evolution

Table captions

Table 1. Compiled features of the Permian Ni–Cu deposits (occurrences) in the Central Asian Orogenic Belt.

Table 1. Compiled features of the Permian Ni-Cu deposits (occurrences) in Central Asian Orogenic Belt.

Location	Deposit	Zircon Age (σ), Ma	Host rock of Zircon	Surface area (km^2)	Intrusion shape	Rock types associated with mineralization	Sulfide texture	Country rocks	Xenolith	Graphite bearing wall rocks in the region	Reserves (Mt) @ Ni, Cu grades (wt.%)	References
NorthTianshan	Huangshanxi	284 (3)	Gabbro	1.71	Satellite, elongate rhomb	Lherzolite, ol websterite	Disseminated	Lower Carboniferous Gandun group	Carbon-bearing slate	Abundant of carbon-bearing slates	65@0.49 Ni, 0.3 Cu	Wang et al., 1987; Mao et al., 2008; Qin et al., 2011
NorthTianshan	Huangshandong	274 (3)	Ol norite	2.8	Elongate rhomb	Lherzolite, ol websterite, ol gabbronorite, gabbronorite	Disseminated, densely disseminated	Lower Carboniferous Gandun group	Carbon-bearing slate	Abundant of carbon-bearing slates	69@0.52 Ni, 0.27 Cu	Wang et al., 1987; Mao et al., 2008; Qin et al., 2011
NorthTianshan	Huangshannan	278 (2)	Ol gabbronorite	4.22	Elongate rhomb	Lherzolite, ol websterite	Disseminated	Lower Carboniferous Gandun group	Carbon-bearing slate	Abundant of carbon-bearing slates	30@0.4Ni, 0.1Cu	Wang et al., 1987; Mao et al., 2016
NorthTianshan	Xiangshanzhong	279.6 (1.1)	Gabbro	2.8	Dyke like	Pl lherzolite, pl ol websterite, gabbro	Disseminated	Lower Carboniferous Wutongwozi group	Unknown	Abundant of carbon-bearing slates	8@0.5Ni, 0.3Cu	Wang et al., 1987; Mao et al., 2008; Han et al., 2010
NorthTianshan	Tudun	280 (3)	Gabbro	0.98	Chonoliths	Pl lherzolite, gabbronorite	Disseminated	Lower Carboniferous Gandun group	Unknown	Abundant of carbon-bearing slates	5@0.3Ni, 0.2Cu	Wang et al., 1987; Mao et al., 2008; Qin et al., 2011
NorthTianshan	Hulu	282.3 (1.2)	Gabbro	0.75	Chonoliths	Lherzolite, ol websterite	Disseminated	Lower Carboniferous Wutongwozi group	Unknown	Abundant of carbon-bearing slates	18@0.44Ni, 0.37Cu	Sun 2009; Han et al., 2013
NorthTianshan	Tulaergen	~280**	Pl lherzolite	0.005	Dyke like	Pl lherzolite, pl ol websterite	Dense disseminated, net-textured	Upper Carboniferous volcanic rocks	Gabbro, tuff	Minor carbon-bearing slates	24@0.42Ni, 0.27Cu	Mao et al., 2008; Sun, 2009; Qin et al., 2011; unpublished data
NorthTianshan	Baixintan*	278 (2)	Pl lherzolite	2.1	Chonoliths	Pl ol websterite	Disseminated	Ordovician volcanic rocks	Unknown	Unknown	/	Li et al., 2014; Wang et al., 2015
NorthTianshan	Erhongwa*	283 (2)	Olivine gabbro	6.25	Elliptical	Pl lherzolite	Weakly disseminated	Lower Carboniferous Gandun group	Unknown	Abundant of carbon-bearing slates	/	Wang et al., 1987; Sun et al., 2013a
Central Tianshan	Tianyu	280 (2)	Gabbro	0.0056	Dyke like	Lherzolite, ol websterite	Disseminated	Precambrian schist, gneiss	Granite	Absent of carbon-bearing slates, minor black shales	Unknown	Wang et al., 1987; Mao et al., 2008; Qin et al., 2011
Central Tianshan	Baishiquan	284.8 (5.7)	Gabbro	~2	Chonolith plus dyke	Pl lherzolite, gabbronorite	Disseminated, net-textured	Precambrian schist, gneiss	Gneiss	Absent of carbon-bearing slates, minor black shales	29@0.32Ni, 0.24Cu	Wang et al., 1987; Mao et al., 2008; Qin et al., 2011; Su et al., 2010
Beishan	Poyi	269.9 (1.7)	Troctolite	1***	Chonolith	Dunite, wehrlite	Disseminated	Lower Carboniferous Hongliuhe group, Precambrian schist and gneiss	Marble, minor gabbro	Minor carbon-bearing slates	67@0.3Ni	Xue et al., 2016
Beishan	Poshi	284 (2.2)	Olivine gabbro	0.6***	Elliptical	Dunite, wehrlite	Disseminated	Lower Carboniferous Hongliuhe group, Precambrian schist and gneiss	Marble, minor gabbro	Minor carbon-bearing slates	/	Qin et al., 2011
Beishan	Hongshishan*	286.4 (2.8)	Troctolite	6.8	Chonoliths	Dunite, wehrlite, lherzolite	Weakly disseminated	Lower Carboniferous Hongliuhe group	Unknown	Minor carbon-bearing slates	/	Su et al., 2011
Beishan	Luodong*	284 (2.3)	Gabbro	1.5	Rhomb	Dunite, wehrlite, lherzolite	Weakly disseminated	Precambrian schist	Unknown	Minor carbon-bearing slates	/	Su et al., 2011
Beishan	Xuanwoling*	260.7 (2)	Gabbro	7.4	Chonoliths	Dunite, wehrlite, lherzolite	Weakly disseminated	Lower Carboniferous Hongliuhe group	Unknown	Minor carbon-bearing slates	/	Su et al., 2011
Beishan	Bijiashan*	279 (2)	Gabbro	0.7***	Elliptical	Dunite, wehrlite, lherzolite	Weakly disseminated	Lower Carboniferous Hongliuhe group	Unknown	Minor carbon-bearing slates	/	Qin et al., 2011
East Junggar	Kemozibayi*	~280**	Pl ol websterite	<1	Unclear	Pl lherzolite, pl ol websterite	Disseminated	Carboniferous Nanmingshui Formation	Unknown	Abundant of carbon-bearing slates	/	Tang et al., under review
East Junggar	Kalatongke	287 (5)	Norite	0.05	Weakly elongate rhomb, funnel shape	Ol gabbronorite, gabbronorite	Net-textured, Massive ore	Carboniferous Nanmingshui Formation	Tuff, slate	Abundant of carbon-bearing slates	38@0.70Ni, 1.19Cu	Han et al., 2004; Annual resource report of 2011 published by the mining company

*-occurrences, some of these intrusions are still in exploration, **-unpublished data, ***-area for ultramafic units

Table 2. Summary and results of experiments of Fe-Ni exchange between olivine and sulfide.

Table 2. Summary and results of experiments of Fe-Ni exchange between olivine and sulfide.								
Experiment ID	Duration (h)	T (°C)	P (MPa)	log fO_2	ΔFMQ	log fS_2*		
GV52	3	1200	64.6	-7.85	0.4	0.88		
GV115Palu	1	1200	67.7	-7.72	0.53	1.03		
GV115P	1	1200	67.7	-7.95	0.3	0.77		
GV128	1	1200	71.9	-9.03	-0.78	-0.59		
GB91	1	1200	81.2	-7.58	0.66	1.12		
GV159	1	1200	76.5	-6.13	2.11	2.86		
GV160	1	1200	77.8	-6.97	1.27	1.87		
Olivine composition								
Experiment ID	*n*	SiO_2	MgO	FeO	NiO	CaO	Total	Fo
GV52	41	40.61	50.78	10.21	0.04	0.43	101.6	89.9
	σ	*0.21*	*0.69*	*0.6*	*0.03*	*0.19*		
GV115Palu	40	40.76	50.47	9.7	0.04	0.43	101.7	90.3
	σ	*0.22*	*0.4*	*0.3*	*0.02*	*0.14*		
GV115P	32	40.68	50.07	10.18	0.03	0.43	101.7	89.8
	σ	*0.25*	*0.51*	*0.39*	*0.01*	*0.19*		
GV128	31	40.25	46.96	13.56	0.02	0.35	101.2	86.2
	σ	*0.36*	*1.1*	*1.29*	*0.01*	*0.06*		
GB91	50	40.85	49.25	10.74	0.05	0.3	101.3	89.2
	σ	*0.25*	*0.49*	*0.28*	*0.02*	*0.07*		
GV159	8	41.19	49.66	9.88	0.13	0.46	101.3	90.0
	σ	*0.16*	*0.41*	*0.27*	*0.07*	*0.19*		
GV160	8	41.12	49.05	10.43	0.19	0.34	101.1	89.4
	σ	*0.24*	*0.43*	*0.59*	*0.05*	*0.1*		
Sulfide composition								
Experiment ID	*n*	Fe	Ni	Cu	S	O	Total	
GV52	62	54.9	1.8	1.9	36.5	2.4	97.8	
	σ	*0.8*	*0.4*	*0.4*	*0.6*	*0.2*		
GV115Palu	35	55.4	1.7	2.6	35.9	2.4	98.2	
	σ	*0.5*	*0.2*	*0.2*	*0.7*	*0.2*		
GV115P	49	56	1.6	1.8	36.2	2.5	98.1	
	σ	*0.6*	*0.2*	*0.3*	*0.5*	*0.2*		
GV128	48	59.2	0.8	0.9	33.2	4	98.3	
	σ	*0.8*	*0.3*	*0.2*	*0.6*	*0.5*		
GB91	34	53.9	2.2	4.1	36.3	2.8	99.4	
	σ	*0.9*	*0.4*	*0.9*	*0.5*	*0.4*		
GV159	13	55	2.1	2.9	36.4	2.8	99.4	
	σ	*0.7*	*0.3*	*0.4*	*0.3*	*0.5*		
GV160	10	43.8	7	8.1	35.4	1.9	99.6	
	σ	*2.8*	*1.3*	*2.5*	*0.8*	*0.3*		

*fS_2 is calculated from the equation of Mungall and Brenan, 2014; *n* is the number of analyses

1104

1105 Table 3. Compositions of pentlandite, pyrrhotite, and chalcopyrite from the Kalatongke,

1106 Huangshanxi, Huangshannan, Xiangshanzhong, Tudun, and Poyi deposits.

Sample	Deposit	*n*	S	Fe	Co	Ni	Fe/Ni	Total	Co/Ni
Y1-700-25-8	Kalatongke	5	33.2	28.4	1.3	35.8	1.26	98.8	26.9
Y2-528-3-8	Kalatongke	5	33.3	29.0	1.4	35.5	1.22	99.2	25.4
Y2-350-31-2	Kalatongke	5	33.2	30.2	1.4	35.1	1.16	100.0	25.6
Y1-650-30-4	Kalatongke	5	32.9	28.4	1.3	35.6	1.25	98.3	26.8
06-18-919	Huangshanxi	6	32.9	30.3	1.6	34.1	1.13	98.9	20.8
06-04-626.7	Huangshanxi	6	32.8	30.7	1.7	33.3	1.08	98.5	19.4
06-04-651	Huangshanxi	6	33.3	29.9	1.5	34.2	1.14	98.9	22.4
06-04-672.6	Huangshanxi	6	33.4	29.1	1.8	34.3	1.18	98.7	18.8
06-04-711.5	Huangshanxi	6	33.2	29.4	2.0	34.0	1.16	98.6	17.3
06-18-944..3	Huangshanxi	6	33.1	29.5	1.8	34.2	1.16	98.4	19.3
HSN455	Huangshannan	5	33.1	31.9	0.6	33.4	1.05	99.0	59.6
14HSN36	Huangshannan	5	33.0	30.9	0.6	34.0	1.10	98.5	53.0
15-4-7	Huangshannan	5	33.0	30.3	0.7	34.5	1.14	98.6	46.7
ZK3693-279	Xiangshanzhong	7	33.2	32.0	1.7	32.1	1.00	99.0	18.9
ZK3693-296	Xiangshanzhong	5	33.3	31.7	2.1	32.7	1.03	99.8	15.8
ZK3693-308	Xiangshanzhong	5	33.5	31.5	1.8	33.0	1.05	99.8	18.3
ZK36953-341	Xiangshanzhong	5	32.9	31.8	1.8	32.0	1.01	98.5	17.8
TD545-4	Tudun	5	33.2	28.8	1.7	36.1	1.25	99.8	21.2
TD505-2	Tudun	5	33.2	28.0	1.5	37.0	1.32	99.6	24.6
TD545-1	Tudun	5	33.1	28.7	1.8	36.3	1.26	99.9	20.1
ZK11-1-197.5	Tudun	5	33.0	28.4	2.1	36.0	1.27	99.5	17.1
ZK11-1-206.5	Tudun	5	33.2	28.3	2.4	35.5	1.26	99.4	14.8
PYZK23-3-761	Poyi	9	33.3	37.4	0.9	27.3	0.73	98.8	31.7
PYZK23-3-1057	Poyi	6	32.7	32.6	0.7	32.5	1.00	98.5	46.5
PYZK23-3-948	Poyi	5	32.4	33.0	0.7	32.0	0.97	98.1	43.2
n-number of analysis									

1107

1108

1109

1110

1111

1112 Table 4. Compositions of sulfide and olivine of the Kalatongke, Huangshanxi,

1113 Huangshannan, Xiangshanzhong, Tudun, and Poyi deposits.

Sample	Rock type	Scale	Deposit	S*	Pn	Cpy	Po	Ni	Cu	Fe	S	Ni/Cu	$Fe/Ni_{sulfide}$	$Fo_{olivine}$	$Ni_{olivine}$	$Fe/Ni_{olivine}$	KD
				wt.%	vol.%	vol.%	vol.%	wt.%	wt.%	wt.%	wt.%		mol.%	mol.%	ppm	mol.%	
Y1-700-25-8	Ol gabbronorite	Thin section	Kalatongke	1.9	15	19	66	5.6	5.9	50.5	37.3	0.9	9.4	76.7	1728.0	103.0	10.9
Y2-528-3-8	Ol gabbronorite	Thin section	Kalatongke	20.1	4	35	61	1.3	11.4	49.6	37.4	0.1	/	74.7	1313.1	140.6	/
Y2-528-3-1	Ol gabbronorite	Thin section	Kalatongke	10.1	8	9	83	3.0	2.7	55.9	38.1	1.1	19.6	74.8	1214.6	149.2	7.6
Y2-350-31-2	Ol gabbronorite	Thin section	Kalatongke	7.7	9	22	70	3.5	6.8	52.0	37.6	0.5	15.6	76.3	1514.8	114.4	7.3
Y1-650-30-4	Ol gabbronorite	Thin section	Kalatongke	13.2	7	12	80	3.5	3.9	55.0	38.0	0.9	16.5	72.5	1375.6	142.7	8.6
06-04-626.7	Lherzolite	Hand sample	Huangshanxi	3.1	16	11	72	5.8	3.6	52.3	37.5	1.6	9.5	85.9	1088.0	101.7	10.7
06-04-651	Lherzolite	Hand sample	Huangshanxi	0.8	27	15	58	9.4	4.8	47.8	36.7	2.0	5.3	n.a.	n.a.	n.a.	/
06-04-672.6	Lherzolite	Hand sample	Huangshanxi	1.8	13	10	77	4.6	3.1	53.9	37.7	1.5	12.4	85.5	1146.0	96.3	7.8
06-04-711.5	Lherzolite	Hand sample	Huangshanxi	1.4	15	14	70	5.4	4.5	51.9	37.4	1.2	10.1	85.8	921.0	118.7	11.7
06-18-944..3	Lherzolite	Hand sample	Huangshanxi	1.7	15	9	76	5.2	2.9	53.4	37.6	1.8	10.9	81.9**	632.0**	222.0**	20.4
06-18-919	Lherzolite	Thin section	Huangshanxi	4.0	20	11	69	7.0	3.6	51.2	37.2	2.0	7.6	n.a.	n.a.	n.a.	/
06-04-626.7	Lherzolite	Thin section	Huangshanxi	2.5	18	9	73	6.2	2.8	52.6	37.4	2.2	8.9	85.9	1088.0	101.7	11.4
06-04-651	Lherzolite	Thin section	Huangshanxi	1.8	26	21	53	9.3	6.5	46.7	36.6	1.4	5.3	n.a.	n.a.	n.a.	/
06-04-672.6	Lherzolite	Thin section	Huangshanxi	3.1	19	9	72	6.7	2.8	52.3	37.5	2.4	8.2	85.5	1146.0	96.3	11.7
06-04-711.5	Lherzolite	Thin section	Huangshanxi	1.5	13	23	63	4.7	7.4	50.0	37.3	0.6	11.2	85.8	921.0	118.7	10.6
06-18-944..3	Lherzolite	Thin section	Huangshanxi	1.4	15	21	64	5.2	6.7	50.1	37.2	0.8	10.2	81.9**	632.0**	222.0**	21.8
ZK3693-279	Pl ol websterite	Thin section	Xiangshanzhong	1.9	14	28	58	4.6	9.0	48.8	37.1	0.5	11.1	80.2	978.2	150.1	13.5
ZK3693-296	Pl ol websterite	Thin section	Xiangshanzhong	2.3	16	18	66	5.5	5.7	50.9	37.3	1.0	9.7	81.4	1100.0	122.2	12.6
ZK3693-308	Pl ol websterite	Thin section	Xiangshanzhong	3.0	13	12	75	4.6	3.7	53.5	37.8	1.2	12.3	79.0	1249.3	170.0	13.8
ZK36953-341	Pl ol websterite	Thin section	Xiangshanzhong	2.2	11	7	81	3.8	2.2	55.5	37.9	1.7	15.5	78.0	978.2	195.0	12.6
HSN455	Pl lherzolite	Hand sample	Huangshannan	6.6	41	8	51	###	2.4	45.9	36.0	6.0	3.4	n.a.	n.a.	n.a.	/
14HSN36	Ol websterite	Hand sample	Huangshannan	6.1	38	6	56	###	1.8	47.4	36.3	7.3	3.8	n.a.	n.a.	n.a.	/
15-4-7	Pl lherzolite	Thin section	Huangshannan	4.7	45	22	33	###	6.9	40.4	35.2	2.3	2.7	n.a.	n.a.	n.a.	/
TD545-4	Gabbronorite	Thin section	Tudun	13.6	15	2	83	5.5	0.5	55.5	38.0	10.9	10.5	n.a.	n.a.	n.a.	/
TD505-2	Gabbronorite	Thin section	Tudun	13.7	10	7	83	3.6	2.3	55.6	38.1	1.6	16.2	n.a.	n.a.	n.a.	/
TD545-1	Gabbronorite	Thin section	Tudun	8.7	13	9	78	4.9	2.7	54.1	37.8	1.8	11.6	n.a.	n.a.	n.a.	/
ZK11-1-197.5	Pl lherzolite	Thin section	Tudun	1.8	18	21	61	6.8	6.6	48.8	37.0	1.0	7.5	83.0	1239.2	90.0	12.0
ZK11-179.5	Pl lherzolite	Thin section	Tudun	3.0	15	18	67	5.5	5.6	51.0	37.3	1.0	9.8	83.1	1382.8	86.2	8.8
ZK11-1-201	Pl lherzolite	Thin section	Tudun	3.3	14	35	51	5.3	11.3	46.1	36.7	0.5	9.2	83.2	1183.8	106.0	11.5
ZK11-1-206.5	Pl lherzolite	Thin section	Tudun	2.1	13	14	73	4.9	4.4	52.5	37.6	1.1	11.3	83.0	1030.2	123.8	10.9
22-2-838	Wehrlite	hand sample	Poyi	1.4	47	13	40	###	4.1	45.9	35.3	3.2	3.7	n.a.	n.a.	n.a.	/
22-4-867	Wehrlite	hand sample	Poyi	1.7	58	19	22	###	6.0	41.5	34.3	2.7	2.7	n.a.	n.a.	n.a.	/
PYZK23-3-761	Wehrlite	Thin section	Poyi	1.3	56	33	11	###	10.4	37.8	34.4	1.5	2.5	90.0**	2514.5*	31.8**	12.8
PYZK23-3-1057	Wehrlite	Thin section	Poyi	1.8	44	20	36	###	6.2	42.4	35.3	2.3	3.2	90.2**	3300.3*	24.0**	7.5
PYZK23-3-948	Wehrlite	Thin section	Poyi	0.7	44	17	38	###	5.4	43.3	35.3	2.7	3.1	90.5**	2357.3*	32.2**	10.3

S*-sulfur content calculated based on the volume proportion of the XRF image of S, Pn-pentlandite, Cpy-chalcopyrite, Po-pyrrhotite

n.a.-not analyzed; 81.9**-data from Mao et al., 2014 and Xue et al., 2016

/-value has not been calculated due to significant sulfide fractionation or to absent of data

1114

1115

1116

1117

1118

1119

1120

1121 Table 5. Summary of the average compositions of olivine and sulfide for the Ni–Cu

1122 deposits in NW China.

Deposit	Location	Host rock	Olivine composition							Sulfide composition								Data source
			Fo	σ	Ni	σ	Fe/Ni	σ		Ni	σ	Cu	σ	Cu/Ni	σ	Fe/Ni	σ	
			mol. %	mol.%	ppm	ppm				wt.%	wt. %	wt.%	wt.%					
Kalatongke	East Junggar	Ol gabbronorite	76.5	2.2	1327	295	137.4	11.9		3.4	1.4	6.1*	3.0	1.8	1.1	19.2	9.8	This study, Li et al., 2012; Gao et al., 2012; Zhang et al., 2009
Huangshandong	North Tianshan	Lherzolite, Ol websterite	82.5	2.0	1269	194	101.7	16.6		6.1	0.9	2.2	1.1	0.4	0.2	9.1	1.3	Mao et al.,2015; Sun et al., 2013b
Huangshandong	North Tianshan	Ol gabbronorite	73.0	3.0						5.2	2.6					10.4	6.9	Mao et al.,2015; Sun et al., 2013b
Huangshanxi	North Tianshan	Lherzolite	83.5	1.2	1094	260	118.7	25.5		6.8	1.8	2.9	2.6	0.4	0.4	7.4	2.2	This study; Mao et al.,2014a; Zhang et al., 2011
Huangshannan	North Tianshan	Lherzolite, Ol websterite	85.9	1.0	2714	163	37.6	9.8		###	1.1	2.2	1.0	0.1	0.1	2.8	0.30	Mao et al., 2016; Zhao et al., 2016
Xiangshanzhong	North Tianshan	Pl lherzolite, Pl ol websterite	79.5	2.6	1084	162	149.2	26.5		4.6	0.6	5.2*	2.5	1.1	0.6	11.7	1.2	This study; Tang et al., 2013
Tudun	North Tianshan	Lherzolite, Pl lherzolite	83.0	0.7	1379	71	101.3	11.6		5.6	0.7	3.2	1.1	0.6	0.1	7.5	1.9	This study
Tulaergen	North Tianshan	Pl lherzolite	82.4	2.8	1189	251	107.0	18.7		8.8	2.5	3.8	1.5	0.4	0.2	5.7	1.9	Sun, 2009
Hulu	North Tianshan	Lherzolite	83.4	2.3	786	192	167.1	55.5		5.0	1.8	2.5	1.4	0.5	0.3	10.9	3.1	Sun, 2009; Zhao et al., 2016
Tianyu	Central Tianshan	Lherzolite	80.4	0.8	677	83	223.6	35.4		4.0	1.5	4.5	4.4	1.1	1.0	13.6	3.2	Tang et al., 2011
Poyi	Beishan	Dunite, Wehrlite	88.0	1.2	2318	601	30.0	2.4		###	0.6	5.5	2.2	0.4	0.2	3.0	0.2	This study, Xue et al., 2016
Fo=100×Mg/(Mg+Fe), σ-Standard deviation.																		
Sample with sulfur content >1 wt.% is used for 100% sulfide calculation, samples that have experienced sulfide fractionation and percolation were not included.																		
Cu tenors in sulfides was estimated from whole rock Ni, Cu, S contents, where these label with * were calculated from XRF images.																		

1123

1124

1125

1126

1127

1128

1129

1130

1131 Table 6. Coefficients and uncertainty of equation (3) for regression of experimental

1132 measurement of K_D.

1133

$K_D = a + b \cdot C_{Ni} + c \cdot \Delta QFM$		
	Coefficient value	σ
a	9.775	1.105
b	0.416	0.033
c	-4.308	0.440

1134

1135

1136

1137 Table 7. Modeling results of olivine composition and Ni tenor in sulfides during the

1138 fractionation of the parental magma and parameters used in modeling.

	Fractionation								Contamination		
Crystallized phase		Ol	Ol	Ol	Ol	Ol	Ol+Cpx+Pl*	Ol+Cpx+Pl*			
F (%)	100	95	90	85	78	74	78	74	10**	20	Avg Crust*
Magma composition											
MgO (wt.%)	14.91	13.04	11.12	9.05	5.86	3.99	5.86	3.99	13.89	12.86	4.66
FeO (wt.%)	9.31	9.28	9.18	8.98	8.38	7.74	8.38	7.74	8.98	8.66	6.04
Ni in magma (ppm)	583	444	327	203	71	25	134	79	536	496	59
Olivine composition											
Fo in olivine (mol.%)	90.0	89.3	87.8	85.7	80.0	75.0	80.0	75.0	90.2	89.9	
Ni in olivine (ppm)	3500	2934	2287	1826	918	420	918	420	3214	3273	
Ni tenor at different R values(wt.%)											
500	13.3	10.9	8.4	5.6	2.0	0.7	3.8	2.3			
1000	17.2	14.4	11.3	7.7	2.7	1.0	5.2	3.3			
2000	20.2	17.1	13.7	9.5	3.4	1.3	6.5	4.2			
7000		19.8	16.0								
D_{Ni} olivine-silicate	6.0	6.6	7.0	9.0	13.0	17.0	13.0	17.0			
D_{Ni} sulfide-silicate	419	477	529	615	637	729	637	729			

F-fraction of residual liquid after fractionation, Ol+Cpx+Pl*-Olivine, clinopyroxene, and plagioclase fractionation after F=85

Avg Crust*-FeO and MgO concentrations of the average crust are from Rudnick and Gao (2003). **- percentage of crustal contamination

D_{Ni} olivine-sulfide is calculated from the host magma compositions from the previous studies of the Huangshandong, Huangshanxi deposits, using the equation of Li and Ripley (2010)

1139 D_{Ni} sulfide-silicate is calculated based on the equation of Kiseeva and Wood (2013): LogDNi=3.83-0.84*Log FeO, whereas FeO equals $FeO_{magma} / [Fe/(Fe+Ni+Cu)]_{sulfide}$